Engineering Fracture Mechanics 323 (2025) 111207

Contents lists available at ScienceDirect

Engineering Fracture Mechanics

journal homepage: www.elsevier.com/locate/engfracmech

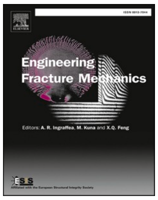

Meshless solution of the crack propagation in brittle elastic material under shear, compressible and tensile loading

Izaz Ali [a], Gašper Vuga [a], Boštjan Mavrič [a], Božidar Šarler [a,b,*]

[a] Faculty of Mechanical Engineering, University of Ljubljana, Slovenia
[b] Institute of Metals and Technology, Ljubljana, Slovenia

ARTICLE INFO

Keywords:
Strong Form LRBFCM
Higher-order Phase Field
Crack Propagation
PHSs
Spectral-split
Strain Decomposition
Shear Test

ABSTRACT

This study explores a robust and computationally efficient two-dimensional solution procedure for phase-field modelling of crack propagation under tensile, compressive, and shear loadings by using the meshless local radial basis function collocation method (LRBFCM). The mechanical model is based on the brittle elastic material, and the crack propagation is governed by the fourth-order phase field equation coupled in a staggered way. The spectral-split method for strain tensor decomposition of a brittle elastic material is used with LRBFCM for crack propagation for the first time. It ensures that the crack is propagated physically correctly under different loading types, filling the gap in our previous study [1], where crack propagation only under tensile loading was possible. The strong-form LRBFCM is constructed on 13-noded subdomains with augmented third-order polyharmonic spline shape functions. A novel adaptive loading step size criterion is introduced to increase computational efficiency by removing cumbersome internal iteration processes. The method's performance is assessed with three benchmark tests subjected to mixed-mode tension, shear and compressive loading. The results are validated with the reference solutions regarding accuracy and convergence rates for scattered and regular node arrangements. The effects of the iterative and non-iterative processes with different loading step sizes are shown.

1. Introduction

The field of fracture mechanics originates from Griffith's pioneering contribution in 1920 [2]. He posted that crack propagation is a competition between the increase in surface energy and the release of elastic energy. The numerical modelling of cracks can be divided into diffuse and discrete approaches. A detailed discussion of these two methods can be found in Egger et al. [3]. Francfort and Marigo, at the end of the last century, introduced a diffuse approach for crack propagation based on the phase field method (PFM) [4]. Initially, in PFM, the pre-defined cracks were considered for initiation of the crack propagation [4], but later [5], it turned out that PFM can also model crack formation and that no pre-defined cracks are required.

The PFM is a generalization of Griffith's theory, which is achieved through the variational minimization of the total potential energy functional [6]. The partial differential equation of the PFM governs the crack propagation. It involves a shape parameter that controls the thickness of the crack [7]. The second-order PFM, also referred to as the standard PFM [8], was used initially for crack propagation [5]. The PFM is computationally expensive, requiring a certain minimum number of discretization nodes over the crack thickness [9]. As a prerequisite for crack propagation, the minimum node spacing in the computational domain must be less than or

---

* Corresponding author at: Faculty of Mechanical Engineering, University of Ljubljana, Slovenia.
E-mail address: bozidar.sarler@fs.uni-lj.si (B. Šarler).

https://doi.org/10.1016/j.engfracmech.2025.111207
Received 28 February 2025; Received in revised form 15 April 2025; Accepted 2 May 2025

Nomenclature

Π	Total potential energy functional
Ω	Domain
Γ	Boundary
ϕ	Phase field
$g(\phi)$	Degradation function
$\psi(\varepsilon)$	Strain energy density
$\boldsymbol{\varepsilon}$	Strain tensor
$\mathbf{C}$	Elasticity tensor
l_0	Length scale parameter
$\mathbf{b}$	Body force
$\mathbf{u}$	Displacement field
$\mathbf{T}$	Traction
G_c	Surface fracture energy
σ	Stress tensor
λ,μ	Lamé parameters
$\overline{\mathbf{u}}$,$\overline{\mathrm{T}}$	Prescribed displacement and traction
Γ_{D},Γ_{T}	Displacement and traction boundaries
$\mathbf{n}$	Outward normal vector
ε_u	Difference in displacement field
ε_ϕ	Difference in PF
$\psi^+(\varepsilon)$,$\psi^-(\varepsilon)$	Tensile and compressive parts of $\psi(\varepsilon)$
tr	Trace
n_d	Number of dimensions
ε	Principal strains (eigenvalues)
$G_{c\mathrm{I}}$	Mode I surface fracture energy
$G_{c\mathrm{II}}$	Mode II surface fracture energy
H^+	History variable
$d(\mathbf{p}, l)$	Nearest distance
$\mathbf{p}$	Any point in the domain
l	Crack line
B	Constant
H_0	Initial history field
f	Arbitrary function
${}_l N$	Number of nodes in the local subdomain
${}_l\Omega$	Local subdomain
${}_l\alpha$	Unknown interpolation coefficients
${}_l\Phi(\mathbf{p})$	Radial basis functions (Shape function)
${}_l\mathbf{p}$	Central node
${}_l\mathbf{p}_i$	Nearest nodes to ${}_l\mathbf{p}$
p_i	Monomials
${}_l\Psi(\mathbf{p})$	Augmented shape functions
M	Number of augmented monomials
a	Highest degree monomial
$\boldsymbol{A}$	Interpolation matrix
${}_l\gamma$	Vector of known values
L	Differential operator
ω_k	Operator coefficients
m	Order of PHS
${}_l h$	Average distance
χ	Auxiliary variable
$\mathbf{D}$	Modified elasticity
∇^s	Symmetric gradient operator
n	Loading step
i	Iteration number
$\delta\phi$	Relative error in phase field
Δu	Loading step size
h	Node spacings

$\xi_{\max}$	Maximum singular value
$\xi_{\min}$	Minimum singular value
κ	Condition number

equal to half of the length scale parameter [5]. Borden et al. [10] proposed a fourth-order PFM in order to relax this requirement of a high number of nodes. The fourth-order PFM contains a square of the Laplacian operator ($\Delta^2\phi$) in the governing equation, which makes the PF solution more regularized with an improved rate of convergence [11]. It guarantees continuous differentiability with a more accurate crack surface than the second-order PFM [12].

Many scientific articles use the fourth-order PFM to showcase its computational efficiency and robustness. An adaptive h-refinement is adopted in [9] to reduce the computational cost and provide continuous and smooth discretization. It is observed in [13] that the fourth-order PFM has a higher accuracy and convergence rate than the second-order PFM. It is also revealed that using only the tensile part of the strain energy can predict realistic crack patterns. In [14], the authors used fourth-order PFM, combined with the cohesive zone model (PF-CZM), for crack propagation in a quasi-brittle material. The fourth-order PF-CZM proposed in [11] can solve strong anisotropic sawtooth fracture. Dynamic crack propagation in hyperelastic materials was successfully solved in [15] using the continuous/discontinuous Galerkin method. In [16], the authors used an adaptive isogeometric-meshfree method, showing that the fourth-order PF can efficiently capture the ductile fracture patterns. A novel approach for PF modelling of crack propagation in brittle and ductile materials based on higher-order nonlocal operators is presented in [17] and [18]. The study in [19] focuses on the computational analysis of crack propagation in a brittle material by combining the finite element and phase-field methods. Another study [20] uses numerical simulations to explore crack propagation in concrete structures. Similarly, the PF modelling of ductile fracture phenomena in [21] aims to study the numerical robustness of the finite element integrations for the ductile fracture analysis. A comparative study of two different computational methods, namely the crack element method and the star-convex approach within phase-field fracture modelling, is provided in [22]. The study [23] discusses the computational analysis to improve the accuracy of PF modelling of brittle fractures by an adaptive refinement strategy. Additionally, the study [24] explores the computational aspects of the PF method for mixed-mode crack propagation in brittle materials. The studies [25–34] are mainly devoted to enhancing the computational aspects of the PF crack propagation. Similarly, other research work on PF crack propagation using the finite element method (FEM) can be found in [19,27,35–37], local maximum entropy approximants in [38] and commercially available software such as COMSOL in [39,40], ABAQUS in [41–44], open-source Gridap; Julia in [45–47] and FENICS in [48–50].

Introducing the energy split method to the PFM [5] was crucial to prevent the non-physical crack formation. Therefore, selecting the suitable energy-split approach is vital because it provides a driving force for crack propagation. It can alter the crack initiation and propagation, specifically during the mixed-mode loading conditions [5]. The volumetric-deviatoric split [51] and the spectral-split [5] methods are the most widely used energy split methods. The main idea behind developing such approaches was to handle the challenges of predicting physically correct crack propagation and the consistency of the material response in different strain states. The tensile and compressive parts of the strain energy density are separated by the volumetric-deviatoric split. The tensile part is degraded and governs crack propagation, capturing the accurate physical properties of the crack [3]. In the spectral-splitting approach, the principal strains and their respective principal directions are considered for calculating the strain energy density. The positive strain energy density (tensile energy) is considered for crack propagation; thus, all non-physical cracks are prevented. A detailed analysis of these approaches is provided in [52].

Solving a higher-order differential equation, like the fourth-order PF equation, is in the context of the FEM very difficult [13] because it requires the C^1 or higher basis functions, which are complicated to construct in the framework of the standard FEM [37]. In meshless methods, it is easy to achieve a high-order approximation space [37]. For example, the fourth-order Cahn-Hilliard PF equation [37] was solved by the reproducing kernel particle method [53], and the isogeometric collocation method [54]. A coupled domain-boundary type meshless method was used in [55] and [56] for PF modeling of dendritic growth with fluid flow. The meshless diffuse approximate method was used to solve the PFM for two-dimensional [57] and axisymmetric Rayleigh-Taylor instability problems [58]. The Element-free Galerkin method, with h-adaptivity, was used for 3D crack propagation using the second-order PFM [59], showing improved accuracy and computational efficiency compared to the case with no h-adaptivity. The robustness and effectiveness of the fourth-order PFM, compared to the second-order PFM, are shown in [12] using the natural element method. The meshless local maximum entropy approximation used in [38] shows that the fourth-order PFM needs fewer nodes to successfully define the crack with a more precise crack surface than the second-order PFM. For the first time, the fourth-order PFM of crack propagation was employed with the strong-form meshless method in [1], showing the efficiency and robustness of the LRBFCM for tensile loading crack propagation.

The LRBFCM [60,61] is one of the most widely used strong-form meshless methods. It calculates the weights of the polynomially augmented RBFs shape functions for each node by applying the collocation on the local subdomains. These weights are then arranged in a global stiffness matrix [62]. Apart from the PF crack propagation, the LRBFCM has been successfully applied to various other problems, such as thermo-elasticity [63], hot-shape rolling process [64], heat diffusion problems [60,61], numerical modelling of visco-plastic material [65], and a solution of the compressible viscous flow in axisymmetric tubes with varying cross-sections [66]. The LRBFCM combined with the augmented polyharmonic spline (PHS) shape functions is used in [62] to simulate small strain elasto-plasticity problems. A numerical model for two-dimensional thermo-elasto-plasticity was proposed in [67] using a hybrid radial basis function finite difference approach. The model was later successfully applied to the cooling bed modelling in the steel manufacturing process [68].

This paper is an extension of our previous work [1], where the fourth-order PFM was used in an isotropic manner to solve crack propagation under tensile loading. In the last work, there was no application of splitting the strain energy density into compressive and tensile parts, which limited the applications to crack propagation under tensile loading only. For the crack propagation under tensile loadings, there is no need to divide the strain history field into tensile and compressive parts [52]. The need to split the strain history field arises during the mixed-mode crack propagation, such as the crack propagation under shear or compressive loading [5,51]. In addition, applying the traction-free boundary conditions for crack propagation under tensile loading was unsuccessful in the previous study [1], while this study presents a successful implementation of the traction-free boundary conditions using the boundary stabilization technique. This paper is based on the hybrid fourth-order PF formulation [52] with the spectral-split [5] decomposition of the strain tensor. It shows the capability of solving crack propagation under shear, tensile and compressive loadings by a local meshless method. In addition, a novel adaptive loading step size criterion is defined to speed up the simulations.

2. Physical model

The governing equations of the hybrid fourth-order PFM are derived using the total potential energy functional Π of a body with a domain Ω and a boundary Γ, under the given boundary conditions [9,10].

$$\Pi = \int_{\Omega}\left[g(\phi)\psi(\varepsilon) + \frac{G_c}{2l_0}\left(\phi^2 + \frac{l_0^2}{2}\Delta\phi + \frac{l_0^4}{16}\Delta^2\phi\right) - \mathbf{b}\cdot\mathbf{u}\right]d\Omega - \int_{\Gamma}\mathbf{T}\cdot\mathbf{u}d\Gamma, \tag{1}$$

where $g(\phi) = (1-\phi)^2$ is a quadratic degradation function, for an isotropic model. The strain energy density is represented as $\psi(\boldsymbol{\varepsilon}) = \frac{1}{2}(\boldsymbol{\varepsilon}:\mathbf{C}:\boldsymbol{\varepsilon})$, where $\mathbf{C}$ is the elasticity tensor, and $\boldsymbol{\varepsilon}$ the strain tensor given as $\boldsymbol{\varepsilon} = \frac{1}{2}\left(\nabla\mathbf{u} + \nabla^{\mathrm{T}}\mathbf{u}\right)$. The parameter l_0 is called the length scale parameter that controls the diffusion of the crack [69] and $\mathbf{b}$ is the body force acting on the material. The term $\mathbf{u}$ is the displacement field, and the prescribed traction on the boundary is defined by $\mathbf{T}$. Additionally, G_c is the surface fracture energy, while ϕ is the phase field that smoothly transitions from the intact material ($\phi = 0$) to completely broken material ($\phi = 1$).

The strong form equilibrium and the PFMs can be derived by minimizing the total potential energy in the equation (1) with respect to $\mathbf{u}$ and ϕ, respectively. By taking $\frac{\partial\Pi}{\partial\mathbf{u}} = 0$ and $\frac{\partial\Pi}{\partial\phi} = 0$ the resultant equations can be written as

$$\nabla\cdot[g(\phi)\sigma] + \mathbf{b} = \mathbf{0}, \tag{2}$$

$$\left(\frac{2l_0\psi(\boldsymbol{\varepsilon})}{G_c} + 1\right)\phi - \frac{l_0^2}{2}\Delta\phi + \frac{l_0^4}{16}\Delta^2\phi = \frac{2l_0\psi(\boldsymbol{\varepsilon})}{G_c}, \tag{3}$$

where the stress tensor σ is defined by the Hooke's law $\sigma = \lambda\mathrm{tr}(\boldsymbol{\varepsilon})\mathbf{I} + \mathbf{2}\mu\boldsymbol{\varepsilon}$, where λ and μ, are the Lamé parameters and $\mathbf{I}$ the second-order identity. The prescribed boundary conditions employed on the boundary $\Gamma = \Gamma_{\mathrm{D}}\cup\Gamma_{\mathrm{T}}$ are

$$\mathbf{u} = \overline{\mathbf{u}}\ \text{on}\ \Gamma_{\mathrm{D}}, \tag{4}$$

$$g(\phi)\sigma\cdot\mathbf{n} = \overline{\mathrm{T}}\ \text{on}\ \Gamma_{\mathrm{T}}, \tag{5}$$

where $\overline{\mathbf{u}}$ and $\overline{\mathrm{T}}$ are the prescribed displacement and traction at Γ_{D} and Γ_{T}, respectively, and $\mathbf{n}$ is the vector pointing in the outward normal direction of Γ.

In the traditional formulation of PF [70], the crack is allowed to propagate even under compressive loads; that is, it cannot differentiate between the tensile and compressive strains during mixed-mode loading conditions. As a result, a physically incorrect crack emerges due to the consideration of the crack propagation also under compressive loadings. To tackle this issue, an energy split method was introduced in [5], which considers only the tensile part of the strain energy density for the crack initiation and propagation.

This study considers the spectral split of the strain energy proposed in [69], in which the tensile $\psi^{+}(\boldsymbol{\varepsilon})$ and compressive $\psi^{-}(\boldsymbol{\varepsilon})$ parts of the strain energy density can be expressed as

$$\psi^{+}(\boldsymbol{\varepsilon}) = \frac{1}{2}\lambda\langle\mathrm{tr}(\boldsymbol{\varepsilon})\rangle_{+}^{2} + \mu\mathrm{tr}\left(\boldsymbol{\varepsilon}_{+}^{2}\right), \tag{6}$$

$$\psi^{-}(\boldsymbol{\varepsilon}) = \frac{1}{2}\lambda\langle\mathrm{tr}(\boldsymbol{\varepsilon})\rangle_{-}^{2} + \mu\mathrm{tr}\left(\boldsymbol{\varepsilon}_{-}^{2}\right), \tag{7}$$

where tr stands for the trace, $\boldsymbol{\varepsilon}_{+}$ and $\boldsymbol{\varepsilon}_{-}$ can be calculated as $\boldsymbol{\varepsilon}_{\pm} = \sum_{i=1}^{n_d}\langle\varepsilon_i\rangle_{\pm}\mathbf{n}_i\otimes\mathbf{n}_i$, n_d is the number of dimensions, ε are the principal strains (defined via tensor eigenvalues) and $\mathbf{n}$ is the normal direction (defined via tensor eigenvectors) of the respective strain tensor. The sign $\langle\bullet\rangle_{\pm}$ defines the operation $\langle\bullet\rangle_{\pm} = \frac{(\bullet\pm|\bullet|)}{2}$, positive for tensile and negative for compressive parts, respectively. The current study considers the hybrid PFM formulation, but it does not impose the condition prescribed in [52]: $\forall\boldsymbol{x}:\psi^{+} < \psi^{-} \Rightarrow \phi := 0$. The strong-form governing equation for PF can be written by modifying the equation (3)

$$\left(\frac{2l_0\psi^{+}(\boldsymbol{\varepsilon})}{G_c} + 1\right)\phi - \frac{l_0^2}{2}\Delta\phi + \frac{l_0^4}{16}\Delta^2\phi = \frac{2l_0\psi^{+}(\boldsymbol{\varepsilon})}{G_c} \tag{8}$$

The crack propagation under mixed-mode loads requires different surface fracture energy. For example, the surface fracture energy for an opening (Mode I) crack G_{cI} could be different than that of shear (Mode II) crack G_{cII} [71]. The modified PFM proposed in [71] considers the combination of G_{cI} and G_{cII} for the calculation of the ratio between G_c and the positive strain energy density ψ^+ defined as

$$\frac{\psi^+(\boldsymbol{\varepsilon})}{G_c} = \frac{1}{2}\frac{\lambda}{G_{\mathrm{cI}}}\langle \mathrm{tr}(\boldsymbol{\varepsilon})\rangle_+^2 + \frac{\mu}{G_{\mathrm{cII}}}\mathrm{tr}\left(\boldsymbol{\varepsilon}_+^2\right) \tag{9}$$

The equation (9) considers Mode I and Mode II contributions to the positive strain energy density. Equations (2) and (8) are fully coupled, and the crack reverses during unloading conditions. Therefore, to decouple it and enforce the irreversibility condition, Miehe et al. in [5] proposed a parameter called the history variable $H^+ = \max\limits_{\tau=[0,t_{\max}]}[2l_0\psi^+(\boldsymbol{\varepsilon}(\mathbf{p},\tau))/G_c]$; in any point $\mathbf{p}$ at the respective loading step τ. By employing the history field in the equation (8), we arrive at the modified strong form of the PFM as

$$(H^+ + 1)\phi - \frac{l_0^2}{2}\Delta\phi + \frac{l_0^4}{16}\Delta^2\phi = H^+ \tag{10}$$

The history field is used to initiate the crack, which is a function of the nearest distance $d(\mathbf{p}, l)$ from any point $\mathbf{p}$ to the crack line l as [51]

$$H_0(\mathbf{p}) = \begin{cases} \dfrac{BG_c}{2l_0}\left(1 - \dfrac{2d(\mathbf{p}, l)}{l_0}\right); & d(\mathbf{p}, l) \leqslant \dfrac{l_0}{2} \\ 0; & d(\mathbf{p}, l) > \dfrac{l_0}{2} \end{cases}, \text{ where } B = \frac{1}{1-\phi} \tag{11}$$

In this study $\phi = 1 - 10^{-3}$ (and corresponding $B = 10^3$) are used in all the simulations. A 2D crack representation of the fourth-order PFM in a cracked body is shown in Fig. 1, with $\phi = 0$ and $\phi = 1$ showing the intact and broken material, respectively.

3. Numerical method and solution procedure

The strong-form meshless LRBFCM [60] solves the governing equations of the decoupled PFM and the mechanical model using a staggered approach proposed in [5]. In LRBFCM, an arbitrary function f with ${}_lN$ nodes in the local subdomain ${}_l\Omega$, as shown in Fig. 2, can be numerically approximated as

$$ {}_lf(\mathbf{p}) \approx \sum_{i=1}^{{}_lN} {}_l\alpha_i\, {}_l\Phi_i(\mathbf{p}), \tag{12}$$

where ${}_l\alpha_i, i = 1, \ldots, {}_lN$ are the unknown interpolation coefficients, which are determined by the collocation and ${}_l\Phi_i(\mathbf{p})$ is an RBF centred at the nearest nodes ${}_l\mathbf{p}_i$ to the central node ${}_l\mathbf{p}$.

To overcome the possible ill-conditioning of the local interpolation problem, the RBFs must be augmented with monomials

$$ {}_lf(\mathbf{p}) \approx \sum_{i=1}^{{}_lN} {}_l\alpha_i\, {}_l\Phi_i(\mathbf{p}) + \sum_{i=1}^{M} {}_l\alpha_{({}_lN+i)} p_i(\mathbf{p}) = \sum_{i=1}^{{}_lN+M} {}_l\alpha_i\, {}_l\Psi_i(\mathbf{p}) \tag{13}$$

where p_i represent the monomials, ${}_l\Psi_i(\mathbf{p}), i = 1, \ldots., {}_lN + M$ describe the augmented shape functions (representing either an RBF or a monomial) with M denoting number of augmented monomials. The M can be calculated as a function of the highest degree monomial a used and the number of space dimensions n_d as

$$M = \frac{(a+n_d)!}{a!n_d!} \tag{14}$$

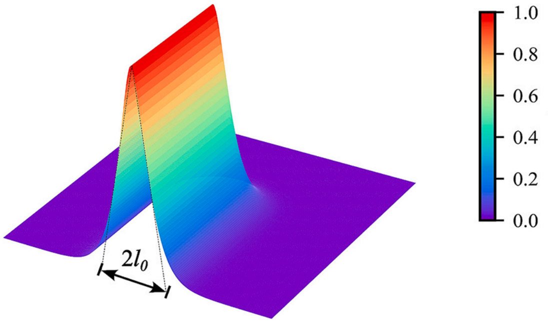

Fig. 1. An example of fourth-order PF variable ϕ with length scale parameter l_0. Values of $\phi = 0$ and $\phi = 1$ represent the unbroken and broken material, respectively.

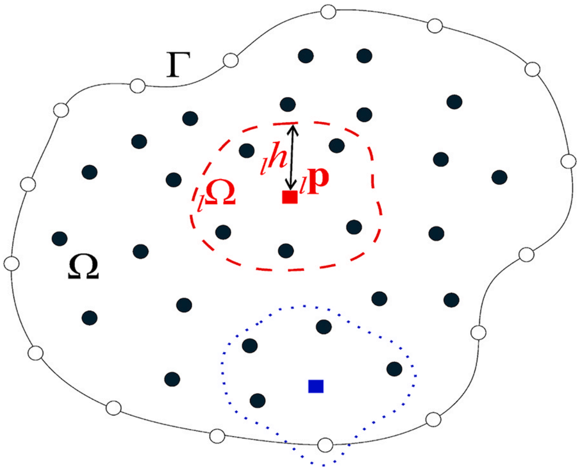

Fig. 2. Computational domain Ω and boundary Γ with solid circles showing the interior nodes and empty circles showing the boundary nodes. The dashed line shows a local subdomain ${}_l\Omega$ containing six interior nodes with the central node ${}_l\mathbf{p}$ represented with a solid square. The dotted line shows a local subdomain containing one boundary node and five interior nodes.

The equation (13) can be written in the form of a system of linear equations as [56]

$$\sum_{i=1}^{{}_lN+M} {}_l\boldsymbol{A}_{ji}\, {}_l\alpha_i = {}_l\gamma_j \tag{15}$$

with the interpolation matrix $\boldsymbol{A}$ consisting of the RBFs and augmented polynomials

$${}_l\boldsymbol{A}_{ji} = \begin{cases} \Psi_i({}_l\mathbf{p}_i) & \text{if } {}_l\mathbf{p}_i \in \Omega \cup \Gamma \\ p_{j-{}_lN}({}_l\mathbf{p}_i) & \text{if } j > {}_lN \text{ and } i \leqslant {}_lN \\ 0 & \text{otherwise} \end{cases} \tag{16}$$

The vector of known values is defined as

$${}_l\gamma_j = \begin{cases} {}_lf\left({}_l\mathbf{p}_j\right) & \text{if } {}_l\mathbf{p}_j \in \Omega \cup \Gamma \\ 0 & \text{otherwise} \end{cases} \tag{17}$$

The application of any linear differential operator $\mathscr{L}$ to equation (13) is given as

$$\mathscr{L}\, {}_lf(\mathbf{p}) \approx \sum_{i=1}^{{}_lN+M} {}_l\alpha_i \mathscr{L}\, {}_l\Psi_i(\mathbf{p}) \tag{18}$$

where the unknown coefficients can be approximated from equation (15) as

$${}_l\alpha = {}_l\gamma_j \sum_{i=1}^{{}_lN+M} {}_l\boldsymbol{A}_{ji}^{-1} \tag{19}$$

from where the equation (18) can be re-written as

$$\mathscr{L}\, {}_lf(\mathbf{p}) \approx \sum_{k=1}^{{}_lN+M} {}_l\gamma_k \sum_{i=1}^{{}_lN+M} {}_l\boldsymbol{A}_{ik}^{-1} \mathscr{L}\, {}_l\Psi_i(\mathbf{p}) \tag{20}$$

In a more simplified form equation (20) can be re-written as

$$\mathscr{L}\, {}_lf(\mathbf{p}) \approx \sum_{k=1}^{{}_lN+M} {}_l\gamma_k\, {}_l\omega_k \tag{21}$$

where the ω_k represent the operator coefficients

$${}_l\omega_k = \sum_{i=1}^{{}_lN+M} {}_l\boldsymbol{A}_{ik}^{-1} \mathscr{L}\, {}_l\Psi_i(\mathbf{p}) \tag{22}$$

3.1. Polyharmonic splines (PHSs) as RBFs

The PHS is a specific type of RBF that has recently received much attention [72,73] due to its easy implementation and user-friendliness with irregular geometries. Unlike the multiquadrics [60], the PHS contain a trivial formula for selecting the shape parameters [61,74]. In the present work, the PHSs are employed as RBFs in the form of

$$ {}_{l}\Phi_{i}(\mathbf{p}) = \left(\frac{\| \mathbf{p} - {}_{l}\mathbf{p}_{i} \|}{{}_{l}h} \right)^{m} \tag{23} $$

with $m = 1, 3, 5, \ldots$ being odd order of PHS. Here we employ $m = 3$, ${}_{l}N = 13$ with $M = 6$ number of augmentation monomials. ${}_{l}h$ is the average distance of the subdomain nodes from the central node as shown in Fig. 2, used as a scaling parameter, which is calculated as

$$ {}_{l}h = \sqrt{ \sum_{i=2}^{{}_{l}N} \frac{\| {}_{l}\mathbf{p} - {}_{l}\mathbf{p}_{i} \|^{2}}{{}_{l}N - 1} } \tag{24} $$

The number of nodes in the local subdomain must be at least twice as large as the number of augmentation monomials to ensure h-convergence, governed by the augmentation order [72,75].

3.2. Solution procedure

The PF and the equilibrium equations are solved in alternating steps, which is referred to in the literature as a staggered approach [4]. The staggered approach solves the PF and mechanical models separately by freezing one while updating the other and vice versa, as shown in Fig. 3. This paper considers the history field initiated crack using the equation (11). Once the history field is defined, the

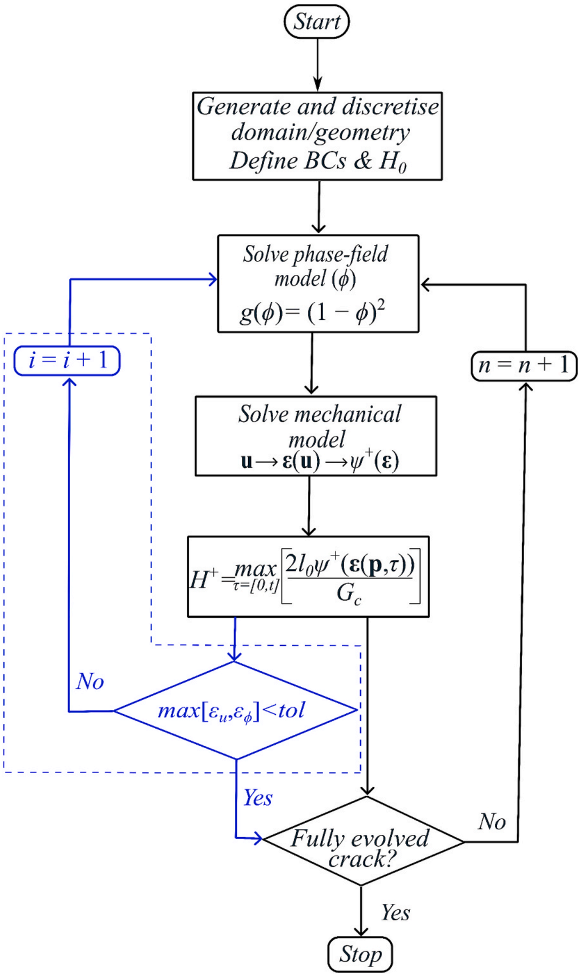

Fig. 3. Solution procedure of the staggered approach. The iterative process is surrounded by the dashed lines.

PFM is calculated to represent the initial crack in the material, utilizing this history field.

The PFM model is solved by introducing an auxiliary variable χ, defined as $\chi = \frac{l_0^2}{2}\Delta\phi$, leading to the effective transformation of the fourth-order PF equation (10) into two second-order partial differential equations as

$$\frac{l_0^2}{2}\Delta\phi - \chi = 0, \tag{25}$$

$$(H^+ + 1)\phi - \chi + \frac{l_0^2}{8}\Delta\chi = H^+ \tag{26}$$

This splitting of the fourth-order PF equation into two second-order equations can also be done in FEM, and low C^p elements could be used to solve the fourth-order PFM. After obtaining the PF, the material stiffness is degraded using the quadratic degradation function $g(\phi) = (1-\phi)^2$. The mechanical model presented in the equation (2), with the degraded material properties, is solved using the composed approach as outlined in [62]. The governing equation (2), can be written as

$$\nabla \cdot [\mathbf{D}\nabla^s]_n \mathbf{u} = -\mathbf{b}_n \tag{27}$$

where $\mathbf{D} = g(\phi)\mathbf{C}$ is the degraded elasticity tensor, $\mathbf{D}\nabla^s = \sigma$ is the stress tensor, and ∇^s the symmetric gradient operator. This linear system of equations is solved for displacement $\mathbf{u}$ at each loading step n. The modified elasticity tensor $\mathbf{D}$ is space-dependent, where the differentiation is achieved by RBFs in combination with PHSs.

The internal iterations within each step are performed to ensure the accuracy of the solution within this staggered setup. The solution procedure with internal iterations is labelled as the iterative process, whereas the convergence is checked for both displacement and PF as

$$\varepsilon_u = \frac{\|\mathbf{u}_{i+1} - \mathbf{u}_i\|}{\|\mathbf{u}_{i+1}\|}, \varepsilon_\phi = \frac{\|\phi_{i+1} - \phi_i\|}{\|\phi_{i+1}\|}, \tag{28}$$

where i is the current iteration number, ε_u is the difference in the displacement field and ε_ϕ is the difference in the PF parameter. The iterative process runs until the difference for both fields fall below the defined tolerance, set to 10^{-4} in this study. A scheme of this process is shown in Fig. 3, with the iterative process highlighted within a blue box. This work also studies the non-iterative solution approach as well. In contrast to the iterative process, in which internal iterations check convergence, the non-iterative process skips these internal steps entirely. The non-iterative process, seen outside the dashed lines in Fig. 3, simplifies the solution by directly updating each model without checking for intermediate convergence. The numerical results show that a non-iterative solution in certain cases provides a faster, albeit less flexible, solution.

Once the displacement is computed, the differential operators obtained with LRBFCM are applied to it to calculate the strain tensor. This strain tensor forms the basis for calculating the strain energy density (the spectral split of the strain tensor is used to calculate the strain energy density). The tensile strain energy density is then utilized to update the history field, which is passed back to the PFM for crack evolution. This alternative exchange of the updated field values is repeated until the material breaks.

3.3. *Adaptive loading step size*

It has been shown in [52] and [1] that there is no need to use the iterative process because the improvement in the results while using the iterative process with a smaller loading step is negligible, thus making the iterative process computationally expensive. To reduce these internal iterations, many articles ([5,9,48]) adjusted the load increment to a smaller value on a hit-and-miss basis, and no valid criterion is defined for adjusting the load increment after a specific time. This article proposes a criterion for adaptive loading step size by calculating the relative error L_2 norm between the initial PF ϕ_{in} and the current PF ϕ as

$$\delta\phi = \sqrt{\frac{\sum_{i=1}^{N} \|\phi_i - \phi_{in,i}\|^2}{\sum_{i=1}^{N} \|\phi_{in,i}\|^2}} \tag{29}$$

The relative error $\delta\phi$, as shown in the equation (29), is then used as a trigger for adjusting the loading step size Δu as

$$\Delta u = \begin{cases} \Delta u_{\text{large}} \ \textit{if}\ \delta\phi < 0.25 \\ \Delta u_{\text{small}} \quad \textit{otherwise} \end{cases} \tag{30}$$

3.4. *Numerical implementation*

The numerical implementation of this method was carried out with Julia (version 1.8.0.). The weights of the coefficient matrix, crucial for the accuracy of the computations, were generated using an in-house library. The simulations in this paper were computed using the AMD Ryzen 9 7950X 16-core processor running at 4.50 GHz.

4. Numerical examples

4.1. Symmetric double-edge crack under tensile loadings

PF is suitable for propagating multiple cracks at the same time. This section discusses a symmetric double-edge crack propagation subjected to tensile loadings, and the coalescence phenomenon is shown. The geometry, boundary conditions and initial PF are given in Fig. 4. The geometry is fixed on the bottom edge, whereas on the top edge, it is free to move in the horizontal direction, while a constant loading increment is applied in the vertical direction. Traction-free boundary conditions are used on the left and right boundaries. The material properties are taken from the reference [43] as $E = 210\left[\mathrm{kN/mm^2}\right]$, $\nu = 0.3$, $l_0 = 0.0075[\mathrm{mm}]$, $G_{\mathrm{cI}} = G_{\mathrm{cII}} = 2.7 \times 10^{-3}[\mathrm{kN/mm}]$. A regular node arrangement with minimum node spacing $h = 0.0037[\mathrm{mm}]$, and a total number of the nodes $N = 36176$ is employed with ${}_{l}N = 13$ subdomain nodes, RBFs of the third-order PHSs and polynomial augmentations with $M = 6$, unless otherwise specified.

4.1.1. Boundary stabilization

It is well-known that, due to the stability issues that emerged because of the oscillations caused by the Neumann boundary conditions, the meshless method applications become limited [74,76–79]. Several techniques have been introduced to treat this boundary stability problem [74,75,77,79–82]. This article utilizes the approach used in [74] to treat the related instability. The gradient operators for Neumann boundary conditions are calculated by shifting the evaluation points in the opposite direction of the outward-facing unit normal vector. The boundary conditions are then evaluated with the gradient operators obtained at the virtually shifted boundary nodes. In this work, the shift size of 0.5 h was selected.

The results of the displacement magnitude over the field after the first loading step, with and without the stabilization, are shown in Fig. 5. Both approaches differ; the solution without stabilization oscillates on the traction-free boundaries due to the sharp gradients. If we proceed with the oscillations, a non-physical crack will eventually emerge, as shown in the first part on the left side of Fig. 5. In contrast, the results with boundary stabilization are smooth and physically correct, as shown in the second part on the right side of Fig. 5. Therefore, it is recommended to use boundary stabilization when dealing with problems related to traction-free boundary conditions. This stabilization technique is used in all the numerical examples in section 4.1.

4.1.2. Comparison with the reference solution

This study’s meshless results are compared with those produced by the second-order PF equation in [43]. Due to the unavailability of the reference solution for the FEM-based fourth-order PFM for this benchmark test, this study used the second-order PFM-based results for comparison.

A constant loading step size $\Delta u = 1 \times 10^{-5}$mm, similar to the one in [43], is used for comparison with the reference solution. The

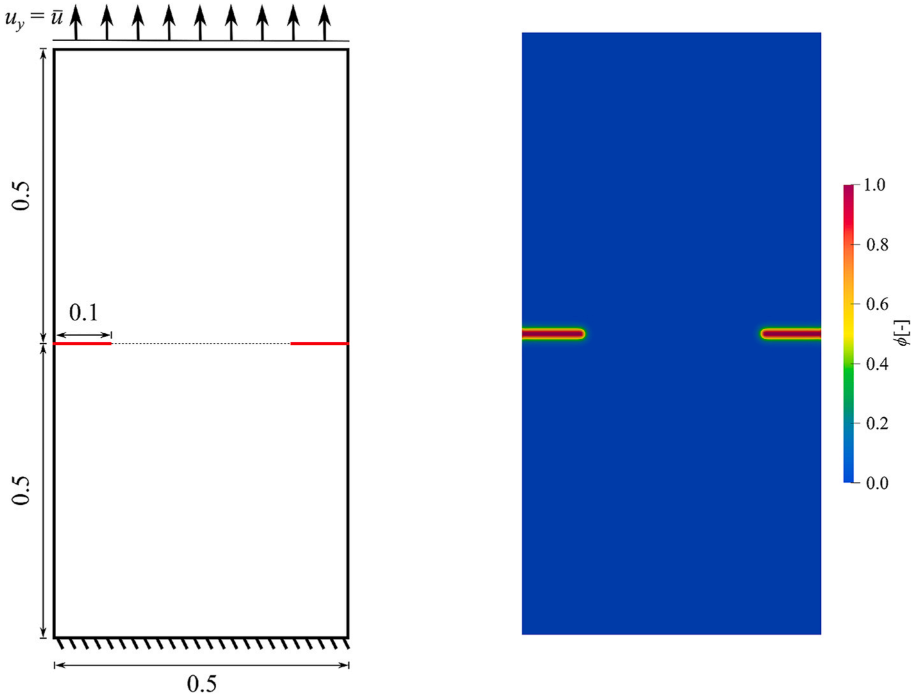

Fig. 4. Geometry, boundary conditions (left), and initial PF (right). All dimensions are in mm.

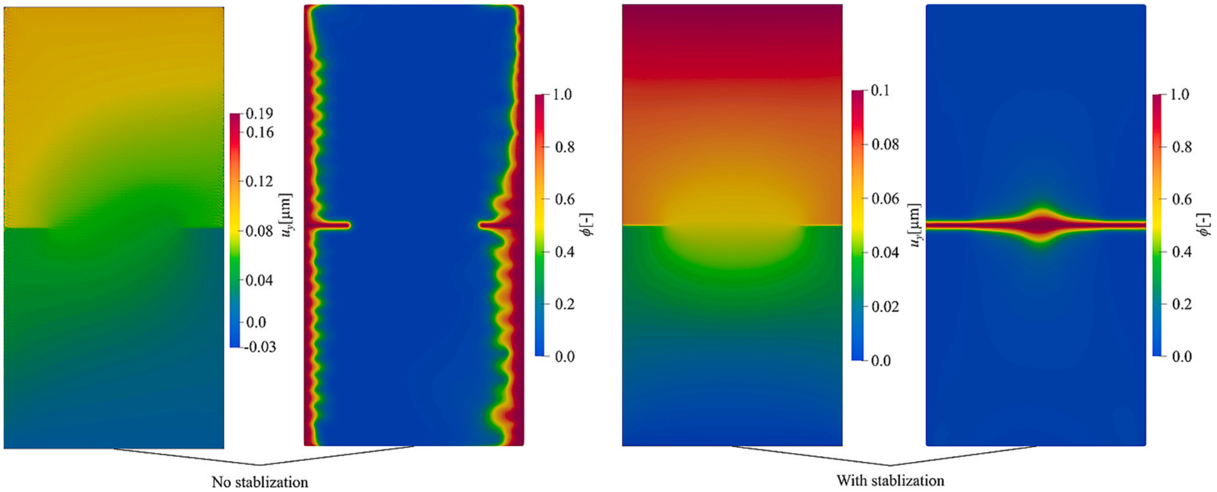

Fig. 5. Displacement and PF evolution after the first loading step (two figures on the left side) and the evolution of the respective fields after the final loading step (two figures on the right side) with and without boundary stabilization, respectively.

force–displacement graphs for the current study and the reference solution are shown in Fig. 6. The results of the present study possess the same slope as that of the reference solution, but the material breaks early with a slightly lower peak load. The lower peak load for the present study occurs because the reference solution is based on the second-order PFM, and it has been reported in [8] that the fourth-order PFM always produces a lower peak load than the second-order PFM. In addition, actual notches are used for the initial cracks in the reference solution with pre-refined mesh in the expected critical zone. In contrast, the present study uses initial history-based induced cracks and uniform node arrangements. The above explanation indicates that the difference in the peak load can be attributed to the variations in the order of the PFM, initial crack representation and node arrangements. The overall trend of the present study is consistent with the reference solution despite all the differences mentioned. The meshless LRBFCM provide consistent results for modelling brittle fracture.

The results in Fig. 6 are produced using the non-iterative process, and a good agreement can still be seen with the reference solution even though the reference solution uses many internal iterations. The non-iterative process with a smaller loading step size is more accurate because the hybrid PFM does not require any internal iteration if a sufficiently small loading step size is used; a similar trend can also be seen in [52]. Another aspect of Fig. 6 is that comparing the results with and without splitting the strain field into compressive and tensile strain energies is identical since, during tensile loading, the entire strain field consists of the tensile strains and the compressive strains make only a negligible contribution. Therefore, the strain decomposition using the tensile loadings does not impact the results. All the simulations in the rest of the paper are done with the spectral-splitting decomposition of the strains unless

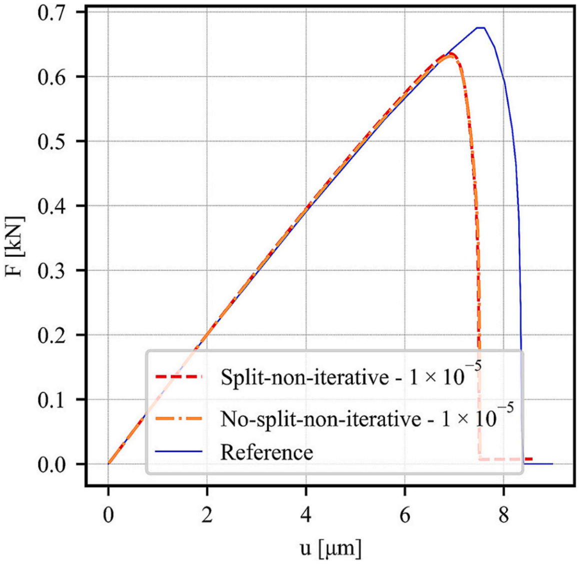

Fig. 6. Comparison of the force–displacement graph with the reference solution [43].

otherwise specified.

The PF evolution after the final step is shown in Fig. 7, where the coalescence phenomenon can be seen at the point where both cracks meet. The PF evolution agrees well with the reference solutions in [43,83].

4.1.3. Effects of the adaptive loading step size

The comparison of different loading step sizes is shown in Fig. 8, where it is clearly shown that as the size of the loading step increases, the peak load increases (i.e. $\Delta u = 1 \times 10^{-4}$mm), and the material breaks in a non-brittle manner, provided that the non-iterative process is used. If the iterative process is used, the peak load decreases, but the computation becomes expensive. Due to the internal iterations, the material stiffness matrix degrades within a single step, resulting in the material's complete failure at a lower peak load than the reference solution, as shown in Fig. 8. If a sufficiently small loading step size is used (i.e. $\Delta u = 1 \times 10^{-5}$mm), then the material breaks in a brittle manner, but again, due to the smaller loading increments, the computational time is high. It can be seen in Fig. 8 that during the elastic region, the slope of all the loading steps is the same. Applying a larger loading step size in the elastic region and then adjusting it with the adaptive loading step size, as explained in section 3.3. the computational time can be reduced significantly. After calculating the $\delta\phi$ from equation (29), the equation (30) is utilized for adjusting the loading step as

$$\Delta u = \begin{cases} 1 \times 10^{-4}[\text{mm}] \text{ if } \delta\phi < 0.25 \\ 1 \times 10^{-6}[\text{mm}] \quad \text{otherwise} \end{cases} \tag{31}$$

Table 1 shows the total CPU time required to complete the simulations with a specific loading step size and the corresponding peak load. The fastest simulation is the one carried out with a non-iterative process and a loading step size of $\Delta u = 1 \times 10^{-4}$mm, but due to the very high peak load and non-brittle nature of the material, this is loading step size is physically incorrect. However, the loading step $\Delta u = 1 \times 10^{-5}$mm is computationally expensive compared to the adaptive loading step size. Therefore, it is recommended to use an adaptive loading step size for better computational efficiency and numerical accuracy.

4.1.4. Comparison of scattered and regular node arrangements

One of the important characteristics of meshless methods is that they can cope with complicated geometry and non-uniform or scattered node distributions [61] that are needed in solving real-world problems. It is essential to test the method's performance for scattered node (SCN) arrangements by comparing it with the regular node arrangements (RGN). This section compares the performance of the proposed method for SCN and RGN with $h = 0.0037$mm.

The force–displacement graphs calculated with RGN and SCN are shown in Fig. 9. Both graphs are in agreement. This agreement of the RGN and SCN results shows that LRBFCM and PHSs as interpolation functions can be used with SCN to simulate crack propagation in any arbitrary complex geometry. The PF and displacement evolution fields at different applied loading for RGN and SCN are shown in Fig. 10. It has been reported in [83] and [43] that using a large loading increment results in a symmetric crack, and the coalescence phenomenon can be observed midway between the two cracks, as shown in Fig. 7 (where a constant loading increment of $\Delta u = 1 \times 10^{-4}$mm was used). In the same studies ([83;43]), it has also been reported that using a smaller loading step size can make the crack

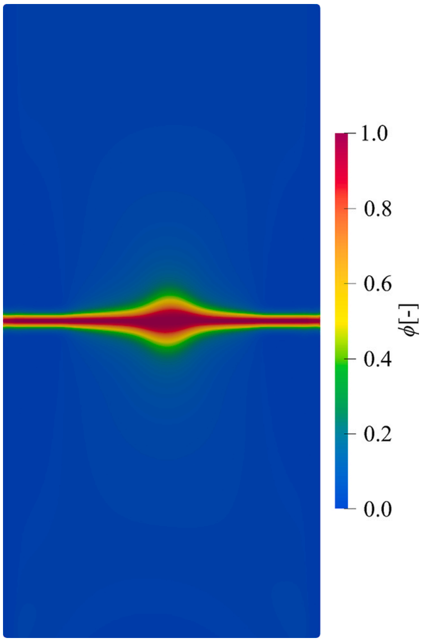

Fig. 7. The final PF solution with the coalescence phenomenon.

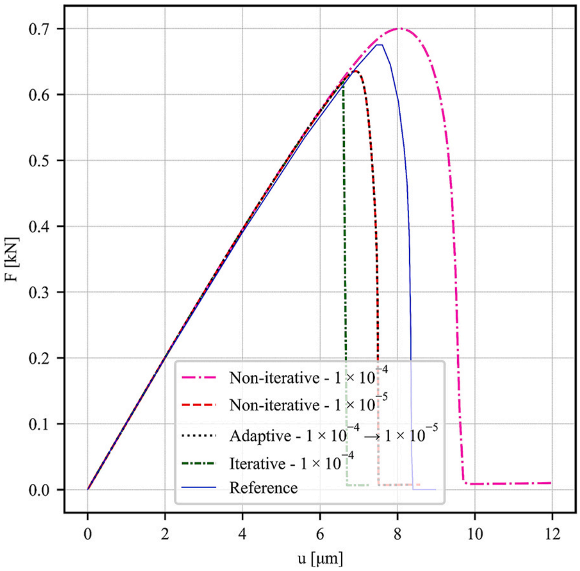

Fig. 8. Comparison of the force–displacement graphs obtained with different schemes of loading steps.

Table 1
Number of iterations taken for the used step sizes and total time taken.

Δu[mm]	Total iterations	Peak load [kN]	CPU time [hrs]
Iterative 1 × 10^{-4}	541	0.62	3.00
Non-Iterative 1 × 10^{-4}	120	0.70	0.40
Non-Iterative 1 × 10^{-5}	857	0.63	4.25
Non-iterative-adaptive 1 × 10^{-4}→1 × 10^{-5}	250	0.63	1.10

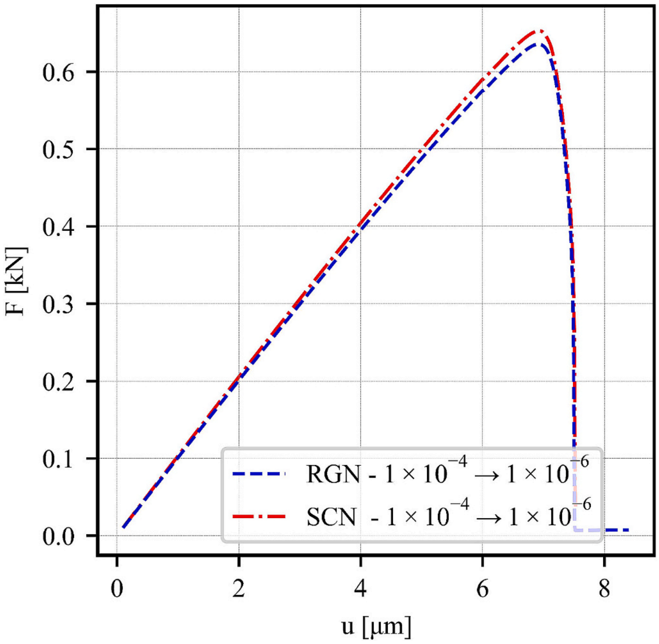

Fig. 9. Comparison of the force–displacement graphs obtained with adaptive loading step size for RGN and SCN.

asymmetric. A similar phenomenon can be observed in this study for both RGN and SCN with adaptive loading steps, as shown in Fig. 10. The simulation in this section was initiated with the loading increment $\Delta u = 1 \times 10^{-4}$mm, and then the adaptive step size criterion (31) was used to reduce it to $\Delta u = 1 \times 10^{-6}$mm. Due to the numerical artefacts, the crack starts propagating from the tip of one crack and reaches the other crack. Another valid reason is that decreasing the loading increment makes the stress distribution uneven, which makes the resulting strain energy density higher on the tip of one crack and lower on the other crack tip. As a result of this uneven strain density, the crack starts propagating from one crack and reaching the other, as shown in Fig. 10.

4.1.5. *h-convergence for displacements in space*

A convergence test is carried out regarding the displacement field in space to check the proposed method's performance. A relative L_2 error norm is calculated for the displacement field with various node arrangements. The reference solution is calculated with the smallest node spacing $h = 0.0033$ [mm], and $l_0 = 0.04$[mm] for all the simulations in this section. The relative error is defined as

$$e_2 = \sqrt{\frac{\sum_i^N \|u_i - \widehat{u}_i\|^2}{\sum_i^N \|\widehat{u}_i\|^2}}, \tag{32}$$

where $\widehat{u}$ is the solution with the smallest node spacings (reference solution in this case) and u represents the solution with gradually increasing node spacings. The relative error is calculated after interpolating the data $(\widehat{u})$ obtained with the smallest h to the respective coarse nodes. Fig. 11 shows the convergence plot by plotting the relative errors against different node spacings. A second-order-convergence line $O\left(h^{2.0}\right)$ is also plotted for reference, and the results for both RGN and SCN show a second-degree convergence rate. Despite using the boundary stabilization method, a second-degree convergence rate is observed even though it is reported in [74] that due to the boundary stabilization, the method loses one degree of convergence compared to the order of augmentation. The results for SCN show a slightly larger error than RGN, but still, the difference with RGN is small, and SCN behaves similarly to RGN.

4.2. *A single-edge crack under shear loadings*

The single-edge cracked square plate subjected to shear loading is one of the most widely used benchmark tests to validate the performance and implementation of the PFM, especially during mixed-mode loading conditions. Due to the shear loading, the need to split the strain energy density becomes prominent because otherwise, physically incorrect crack propagation occurs. The geometry and

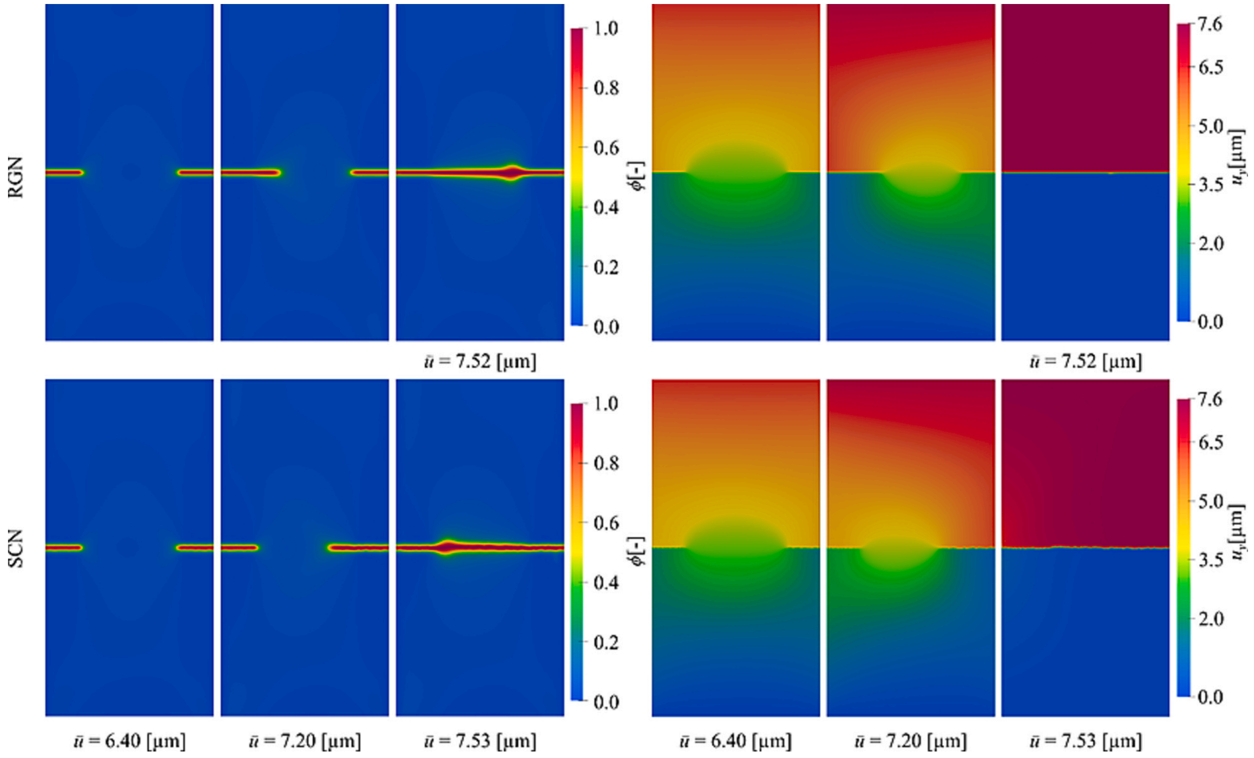

Fig. 10. PF (left) and displacement field (right) evolution for RGN (top) and SCN (bottom) at the respective applied load.

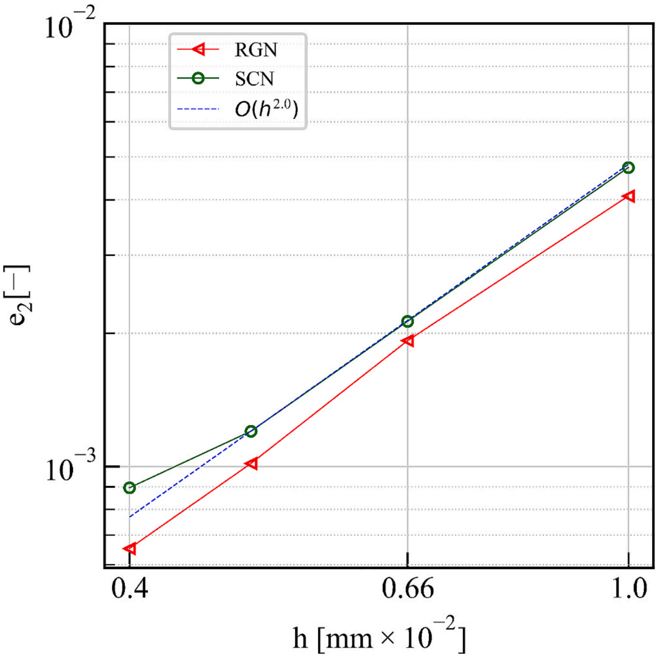

Fig. 11. h-convergence for displacement in space for RGN and SCN.

boundary conditions are shown on the left side, whereas the history field initiated crack in the domain is shown on the right side of Fig. 12. For a pure shear case, the domain is fixed at all boundaries in the y-direction, fixed at the lower edge in both the x- and y-directions, and a load at increment n is defined for u_x on the top boundary as $\overline{u}_n = \overline{u}_{n-1} + \Delta u$. In order to test the performance of the proposed meshless method, the material properties are taken the same as used in [69,84–86]: $\lambda = 121.15\left[\text{kN/mm}^2\right]$, $\mu = 80.77\left[\text{kN/mm}^2\right]$, $G_{cI} = G_{cII} = 2.7 \times 10^{-3}[\text{kN/mm}]$ and $l_0 = 0.015[\text{mm}]$. A regular node distribution with minimum node spacing $h = 0.00625[\text{mm}]$ and a total of $N = 25596$ nodes are used for the simulations. The number of nodes used in the local subdomain are ${}_lN = 13$. The augmentation employs six monomials $M = 6$. These material properties and simulation parameters are used in all the simulations carried out in the section 4.2., except mentioned.

4.2.1. Comparison with the reference solution

In this section, the results were obtained using a constant loading step of $\Delta u = 10^{-5}[\text{mm}]$ with an iterative process, as shown in Fig. 3. The results of the present study are compared with the reference solution [85,86]. The reference solution from [85] is referred to as “Yu et al.,” the reference solution from [86] is referred to as “Weinberg et al.,” and the reference solution from the paper [87] is referred to as “Li et al.,” as shown in Fig. 13. The results from both the reference solutions (Yu et al. and Weinberg et al.) were obtained using the fourth-order PFM, whereas Li et al. is based on the second-order PFM. In Yu et al. and Li et al., a pre-refined mesh at the

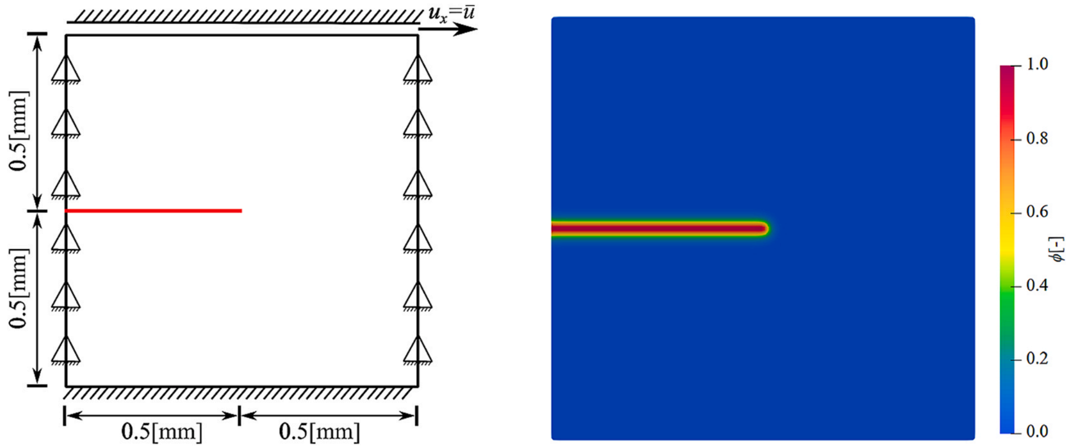

Fig. 12. Geometry and boundary conditions under pure shear loadings (left) and the initial PF (right).

expected crack path and an actual notch are used, and additionally, Yu et al. used an adaptive loading step from 1×10^{-4}mm to 1×10^{-5}mm. In contrast, the Weinberg et al. used 256×256 uniform isogeometric elements with a mesh-induced (actual notch) initial crack and a constant loading step of 10^{-6}[mm] in their simulations.

The reason for comparing our meshless method results with two different reference solutions is to show that the PFM of crack propagation depends on many aspects like mesh density, loading increment, length scale parameter and numerical method used to solve the PF governing equation. A similar trend of the deviation of the results was also reported in [88] and [84]. Due to the reasons above, the results of the present study don't match the reference solutions precisely, but they are still in reasonably good agreement. The trend of the current study is more similar to the results of Yu et al.. It can be seen that after the peak load is approached, the material breaks abruptly, showing a more brittle nature of the material.

4.2.2. *Effects of splitting the strain history field*

The model without splitting the strain history field into compressive and tensile parts is called the isotropic model, referred to as a no-split model here. Here, the effects of the strain history field with and without splitting are discussed in detail. This article uses the spectral split, proposed by Miehe et al. in [69], for splitting the strain history field into compressive and tensile strain history fields. The tensile part of the strain history field is used as a driving force for crack growth in the PFM. The force–displacement graph for both approaches is shown in Fig. 14, whereas the PF evolution is shown in Fig. 15. Fig. 15 shows an unphysical crack evolution that emerges using the no-split approach. This non-physical crack propagation occurs because, during the no-split approach, the PF driving force cannot differentiate between the compressive and tensile strains, and that's why crack propagation occurs even at the compressive strains. The spectral-split approach will be used for the rest of the simulations in this paper.

4.2.3. *Effects of the internal iterations*

The process with internal iterations is referred to as the iterative process, and the process without internal iterations is referred to as the non-iterative process. The force–displacement diagram for the iterative and non-iterative processes is shown in Fig. 16. If the iterative process is used, a large loading step produces the same results as a smaller one. If a large loading step is used, the material will reach the peak load quickly, thus saving significant computational time. The number of iterations required for each loading increment is shown in Fig. 17. It can be seen that the number of iterations necessary for a smaller loading increment, that is $\Delta u = 1 \times 10^{-5}$mm, is much larger than that for a larger loading increment, that is $\Delta u = 1 \times 10^{-4}$mm. The number of iterations required, the peak load, and the time needed for both iterative and non-iterative processes until the material breaks are shown in Table 2. It can be seen that a large number of iterations are required while using a smaller loading increment, whereas using a larger loading increment needs relatively less time with approximately the same peak load value. Fig. 16 shows that during the elastic region, even if we use a larger loading step with either an iterative or non-iterative process, the force–displacement diagrams overlap each other, showing no change in the elastic region. A significant change can be seen with different loading increments for the non-iterative process as soon as the peak load approaches. Still, with the iterative process, a negligible difference can be seen in the peak load. It is also clear that by using a larger loading step, the material breaks in a non-brittle manner, and by decreasing the loading step size, the material behaves physically more correctly and approaches the iterative process in terms of the peak load.

Additionally, the convergence behaviour of the PF parameter and displacement field, with a horizontal tolerance line at 10^{-4}, during the iterative process is shown in Fig. 18. The relative difference presented in eq. (28) is plotted in a log scale on the vertical axis,

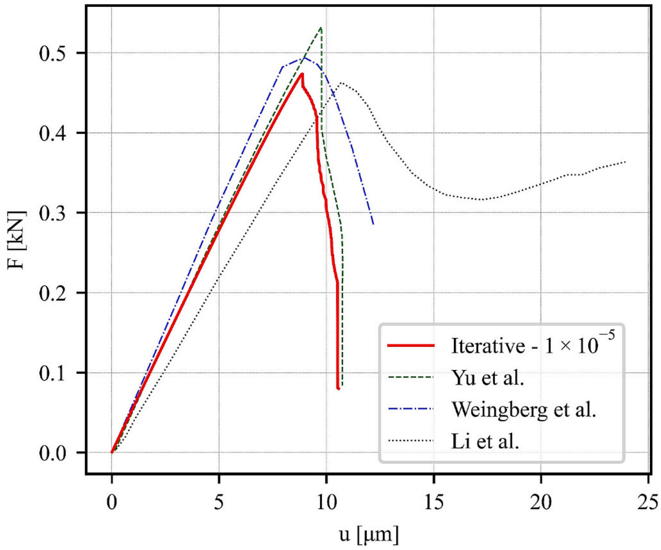

Fig. 13. Comparison of the force–displacement diagram obtained with our method (solid curve) with "Yu et al." from [85], "Weinberg et al." from [86] and "Li et al." from [87].

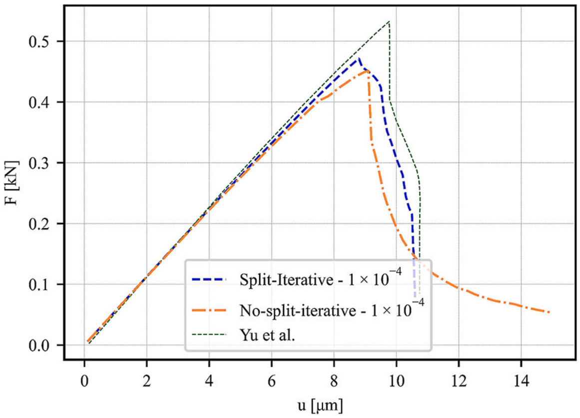

Fig. 14. Comparison of the force–displacement diagram for splitting and non-splitting strain history field.

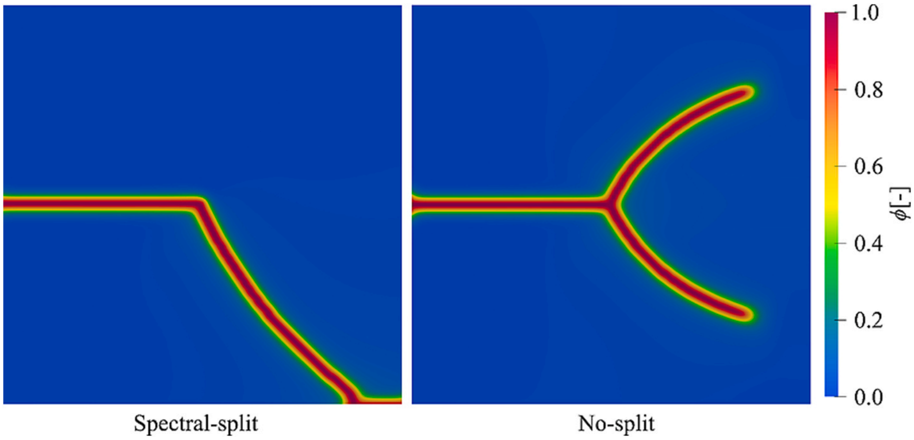

Spectral-split No-split

Fig. 15. Crack evolution with spectral split (left) and no split (right) strain history field.

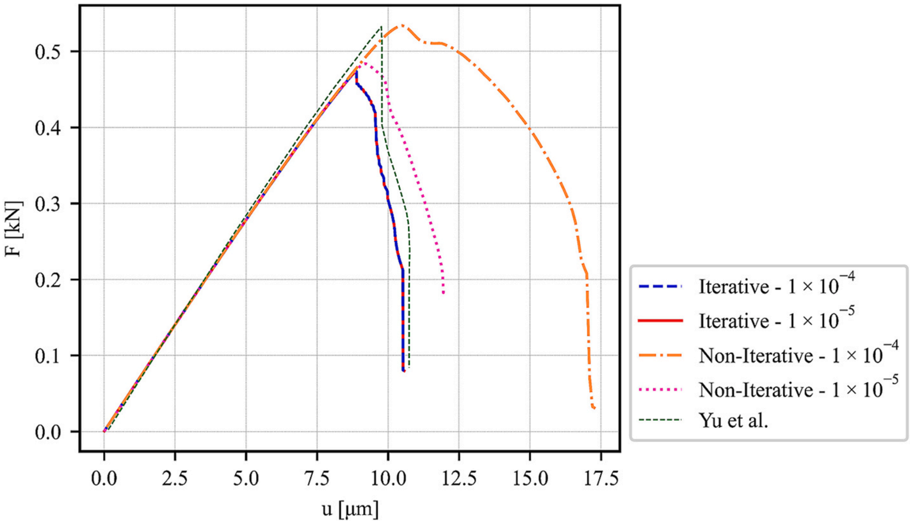

Fig. 16. Effects of the iterative and non-iterative process with $\Delta u = 1 \times 10^{-5}$mm and $\Delta u = 1 \times 10^{-4}$mm showing the loading increment used in the respective process.

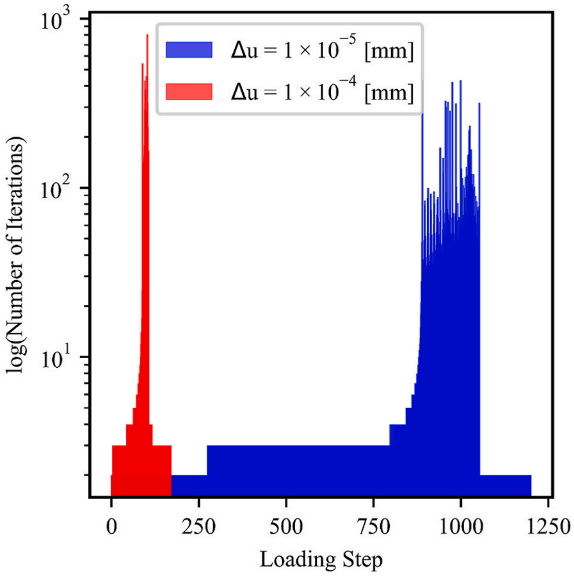

Fig. 17. The number of iterations required for each loading increment.

Table 2
Number of iterations at the used step size and total CPU time.

Δu[mm]	Total iterations	Peak load [kN]	CPU time [hrs]
Iterative 1×10^{-4}	6049	0.45	18
Iterative 1×10^{-5}	17,246	0.47	51
Non-iterative 1×10^{-4}	170	0.53	0.34
Non-iterative 1×10^{-5}	1198	0.48	3.41

while the cumulative iterations are plotted on the horizontal axis. The loading increment used in the generation of Fig. 18 is $\Delta u = 1 \times 10^{-4}$mm. A new loading increment is applied as soon as the difference in both the PF variable and displacement field falls below $tol \leqslant 10^{-4}$. The repeated sawtooth-like pattern shows the iterative process in each loading step; the difference is high at the beginning of each loading step and eventually decreases as the internal iterations increase. Interestingly, the displacement field converges faster than the PF parameter; thus, the PF parameter dictates the required number of iterations for the convergence process. At the beginning of the simulations (before loading step 88), the PF parameter and displacement field converge in a few iterations because there is no crack propagation, and the PF parameter has a smaller value. At the end of the simulations (after loading step 120), both the PF parameter and displacement field show a sharp drop in the difference and converge in a few internal iterations, indicating a complete failure of the material.

4.2.4. *Effects of the adaptive loading step size*

It is shown in Table 2 that the non-iterative process with $\Delta u = 1 \times 10^{-5}$mm is closer to the iterative process, and it is much faster compared to the solution with the iterative process. Fig. 16 shows that the loading increment does not affect the results during the elastic region; i.e. a larger loading step size can be utilized before the peak load.

The initial loading step size is taken as $\Delta u = 5 \times 10^{-4}$mm , and then decreased adaptively to $\Delta u = 1 \times 10^{-6}$mm by calculating $\delta\phi$ from equation (29) and the equation (30) becomes

$$\Delta u = \begin{cases} 5 \times 10^{-4}\text{mm if } \delta\phi < 0.25 \\ 1 \times 10^{-6}\text{mm} \quad \text{otherwise} \end{cases} \tag{33}$$

The results of the adaptive loading step size PFM are shown in Fig. 19, and the respective CPU timing is given in Table 3; it can be seen that the result of the PF with the adaptive loading step size is much closer to the reference solution and also closer to the iterative process with $\Delta u = 1 \times 10^{-5}$mm. On the other hand, even though the adaptive approach is carried out with a non-iterative process, the material still breaks in a brittle manner, unlike the non-iterative process with a constant loading step, which breaks in a non-brittle nature.

4.2.5. *Comparison of scattered and regular node arrangements*

The adaptive loading step size with a non-iterative process, as shown in the equation (30), with minimum node spacing, $h =$

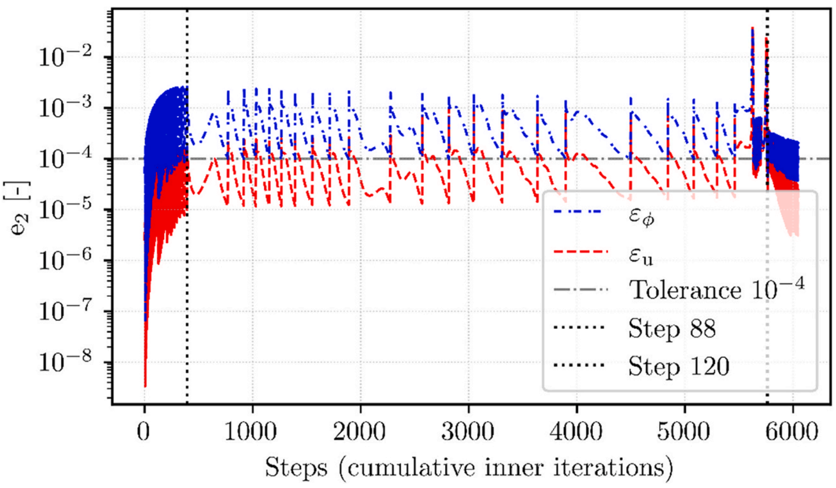

Fig. 18. Convergence history of ϕ and u during the cumulative inner iterations of the iterative process.

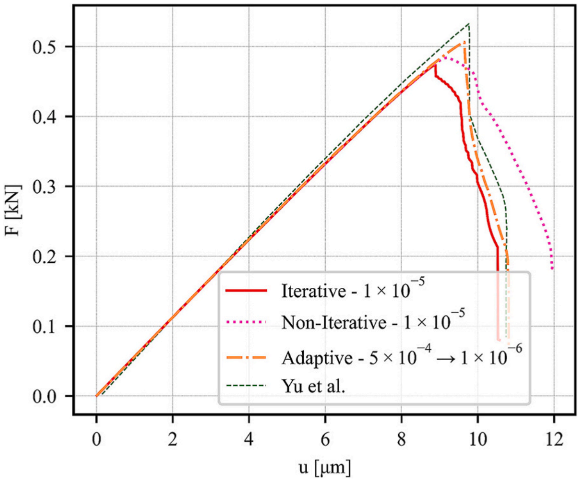

Fig. 19. Comparison of the adaptive loading step size model with the iterative process and the reference solution from [85].

Table 3
Number of iterations, peak load and CPU time as a function of the step size approach.

Δu[mm]	Total iterations	Peak load [kN]	CPU time [hrs]
Iterative 10^{-4}	6049	0.45	18
Iterative 10^{-5}	17,246	0.47	51
Non-iterative-adaptive $5 \times 10^{-4} \rightarrow 1 \times 10^{-6}$	1193	0.50	4

0.00625[mm] is used for both SCN and RGN. The material and numerical parameters are the same as in the previous sections. The force–displacement diagram for SCN and RGN is shown in Fig. 20. The SCN results agree with the RGN, showing that the method is well-suited for complicated crack patterns because it can perform well while using SCN.

A condition number (κ) is calculated for the final global stiffness matrix of the mechanical model to check the conditioning behaviour of the proposed method as

$$\kappa = \frac{\xi_{\max}}{\xi_{\min}} \tag{34}$$

where $\xi_{\max}$ and $\xi_{\min}$ are the maximum and minimum singular values. The condition number is calculated with various node densities for SCN and RGN after the first loading step, and the results are plotted on a log–log scale against the minimum node spacing, as shown in Fig. 21. The condition number is inverse to the minimum node spacing, i.e., as the node spacing decreases, the condition number

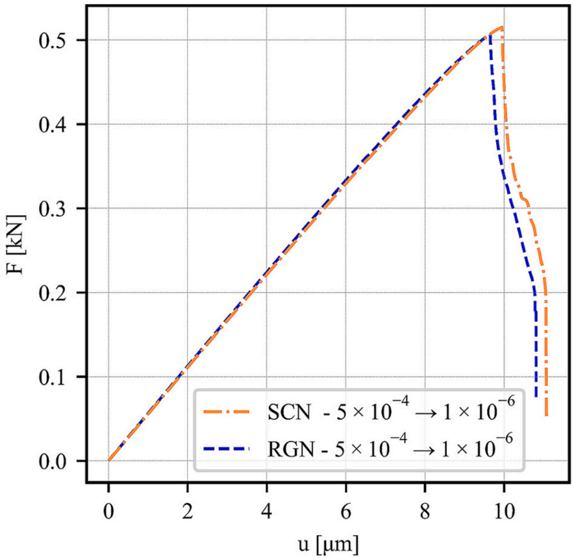

Fig. 20. Force-displacement graph for RGN and SCN with adaptive loading step size.

increases. This behaviour is expected in the RBF-based methods, as reported in [89], that even though the condition number for PHS as RBFs is higher, the interpolants do not suffer instability because of this ill-conditioning. Similar results are explained in detail in [90] for the relationship between the node density and the condition number. Another study [74] also calculated the condition numbers, which fall in the same range as in this study. Therefore, the condition numbers of the RGN and SCN distributions are in the range, so solving complex problems like crack propagation is possible using the LRBFCM.

The PF and displacement magnitude evolution under different loading steps for the SCN and RGN are shown in Fig. 22 and Fig. 23, respectively. A similar PF crack propagation contour plot can be seen widely in the literature [9,49,51,69].

4.2.6. *h-convergence for displacements in space*

A relative L_2 error norm is calculated for the displacement field with various node arrangements using the equation (32). The reference solution is calculated with the smallest node spacing $h = 0.004[\mathrm{mm}]$ and $l_0 = 0.04[\mathrm{mm}]$ for all the simulations in this section. Fig. 24 shows the convergence plot using RGN and SCN. As expected, the convergence rate is approximately $O\left(h^{2.0}\right)$, showing that the augmentation order governs the convergence rate.

4.2.7. *Computational cost*

The computational cost at different simulation stages is recorded using various node densities (100 × 100, 160 × 160, and 200 × 200). The computational cost is divided into the average time required for the stiffness matrix assembly for the mechanical and PF

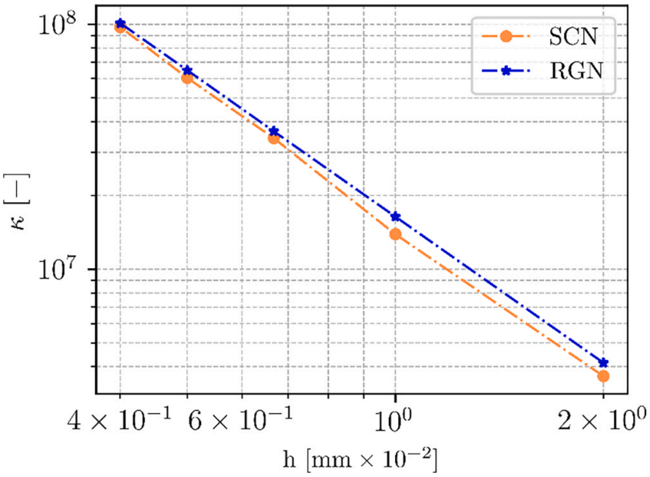

Fig. 21. Condition number as a function of minimum node spacings.

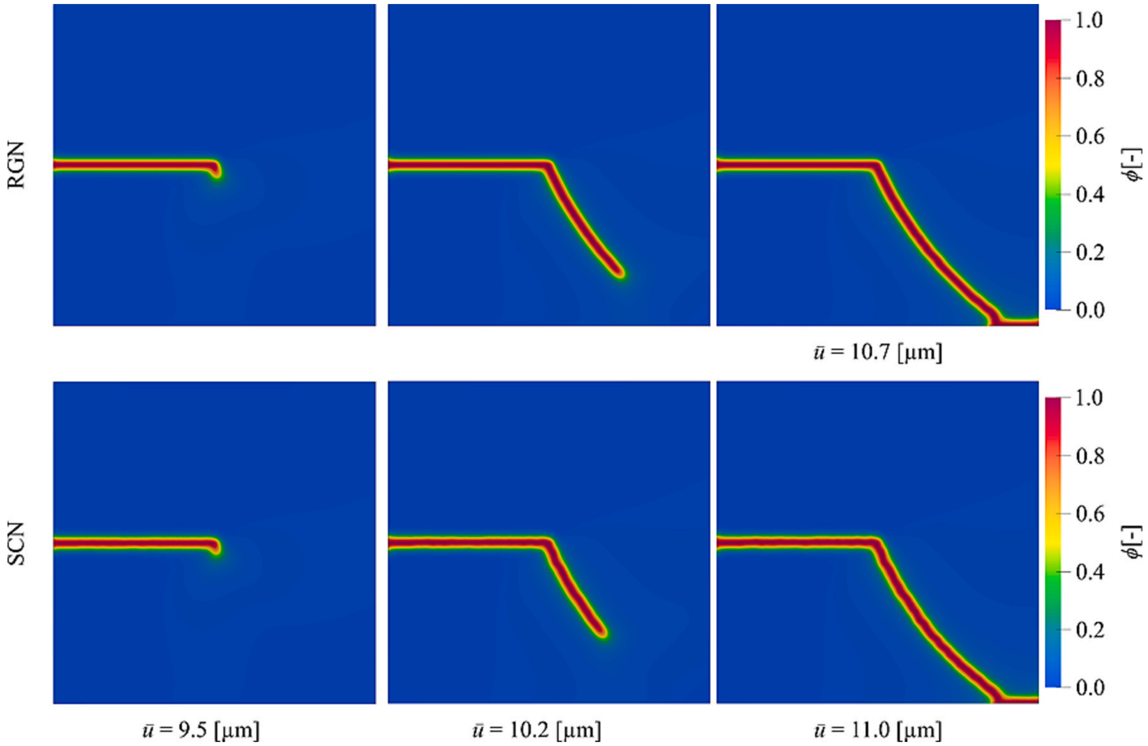

Fig. 22. PF evolution for RGN and SCN at the respective applied load.

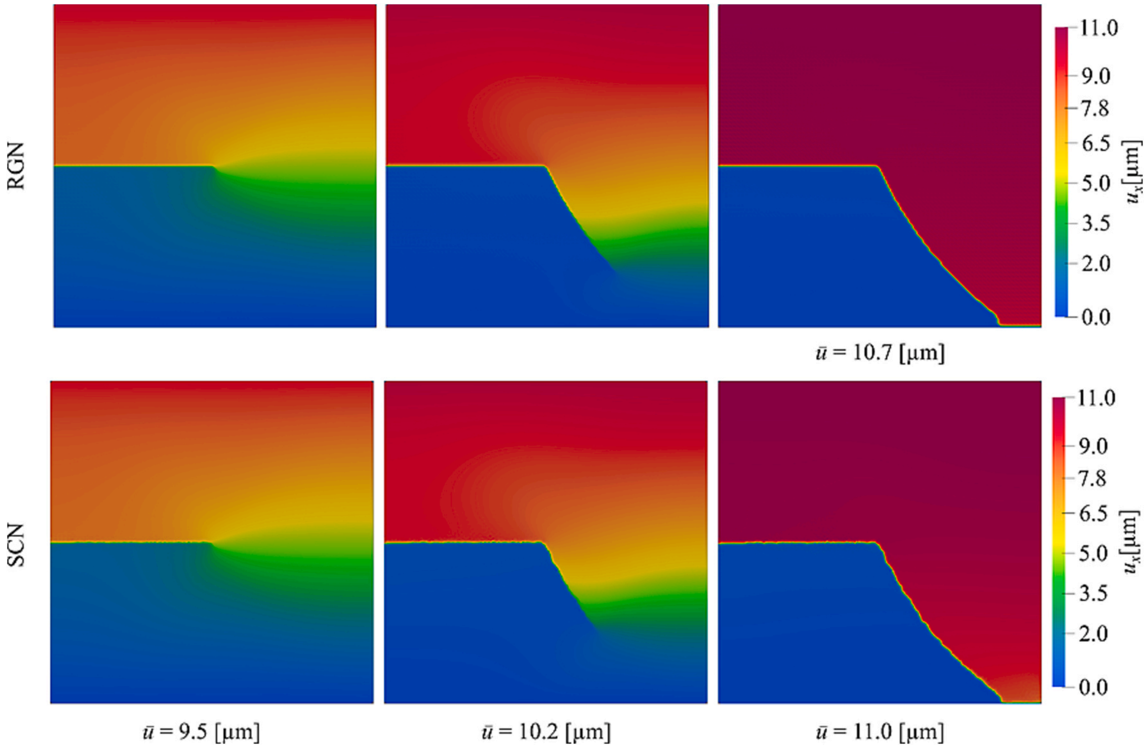

Fig. 23. Displacement field evolution for RGN and SCN at the respective applied load.

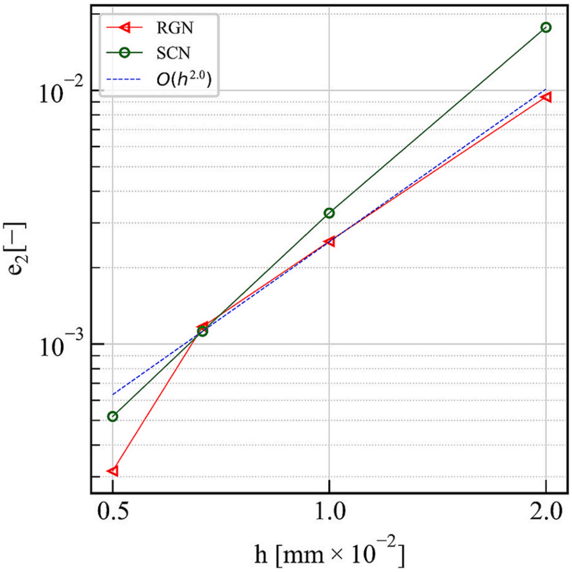

Fig. 24. h-convergence for displacement calculated with RGN and SCN.

models and then the solution of the assembled stiffness matrices, as shown in Fig. 25. In Fig. 25, the most dominant is the assembly of the mechanical matrix, followed by the time taken for the solution of the mechanical model. These results highlight the computational cost of the proposed approach, which increases as the node density increases, even in a 2D setting.

Extending this approach to a 3D case would significantly increase the computational cost because the number of nodes will grow cubically. Therefore, the matrix operations will become more complex and require a large memory. However, implementing a 3D case may require adaptive refinement of nodes near the critical regions susceptible to crack growth. The adaptive node refinement is outside the scope of this study but is an essential direction for future work, which will be considered in future studies.

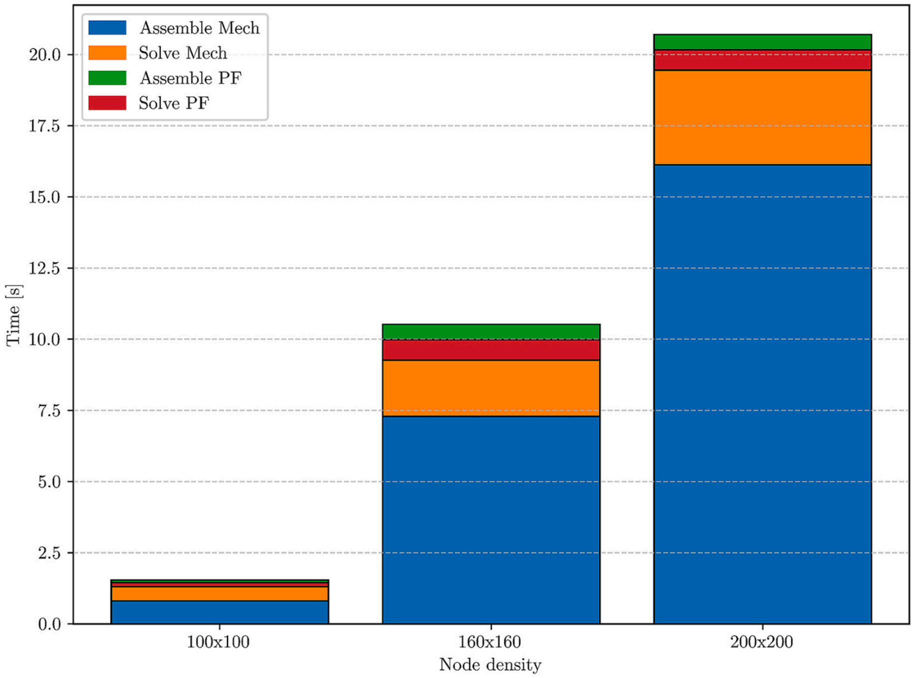

Fig. 25. Computational time required for different stages of the simulation with various node densities.

4.3. A rectangular plate with a centrally inclined crack subjected to compressive loads

The crack propagation under compressive loads is essential because it provides valuable insights into the failure mechanisms of the materials subjected to complex loadings in real-world applications. When subjected to compressive loading, the inclined crack experiences a combination of shear and normal stresses. Interestingly, the inclined cracks under compression start propagating in the direction of the applied load [91], which is unusual compared to tensile loading, where the cracks usually propagate perpendicular to the applied load. In the compressive loading on the inclined cracks, the crack experiences an inward force, potentially leading to closing the crack. At the same time, the shear component promotes the sliding and thus, crack extension occurs. In the inclined crack under compression, the compressive stress state dominates [56], so the crack propagates under compressive loading. Experimental [91,92] and numerical studies [71,93,94] have shown that wing-shaped crack propagation, parallel to the applied loading, occurs under compressive loads.

In this section, an inclined crack at 45° to the horizontal axis is studied under the compressive loads, as shown on the left side of Fig. 26, with a PF representation of the initial crack on the right side of Fig. 26. The bottom edge is fixed to move in the vertical direction, and the top edge is fixed to move in the horizontal direction. In contrast, an incremental displacement is applied in the negative vertical direction on the top edge. The material properties are taken from [71] and are used for both RGN and SCN as $E = 650[\text{MPa}]$, $\nu = 0.2$, $\Delta u = 0.1\text{mm}$, $h = 0.4[\text{mm}]$, $l_0 = 2h[\text{mm}]$, $G_{c\text{I}} = 9.1\left[{}^{\text{N}}\!/_{\text{m}}\right]$, and $G_{c\text{II}} = 130\left[{}^{\text{N}}\!/_{\text{m}}\right]$.

The results of the current study obtained with RGN and SCN are compared with the experimental crack path, taken from [71], in Fig. 27. The symmetrical wing cracks are produced with RGN and SCN arrangements, which agree well with the experimental crack path, as shown in Fig. 27. A similar trend of the resultant wing cracks (shown in Fig. 27) of an inclined crack under compressive loading is also reported in [71,91,92].

5. Conclusions

This paper is an extension of the previous study [1], where the application of crack propagation was limited to tensile loading only. This work successfully overcame this limitation using the spectral split to calculate the strain energy density. The present paper shows the first strong-form meshless method solution of crack propagation under mixed-mode shear and tensile loading. The performance of the strong-form meshless LRBFCM with augmented PHS shape functions for solving the PFM coupled with the mechanical model is shown for both RGN and SCN. The mechanical and PF models are coupled in a staggered form, allowing for more flexibility and decoupling of the models. The strain energy density is calculated using the spectral-split decomposition of the strains. The spectral split ensures that the crack propagates only under tensile strains. The strain energy density tensile part is utilized as a crack driving force. An adaptive loading step size criterion is introduced for better computation efficiency. The method's numerical implementation and performance are tested with two benchmark tests.

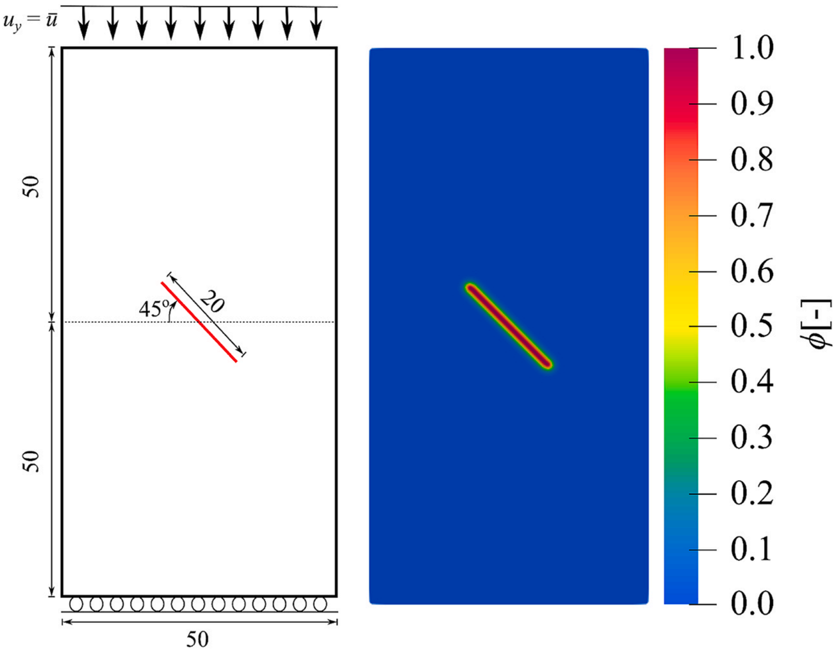

Fig. 26. Geometry and boundary conditions for centrally inclined crack under compressive loads on the left and the initial crack represented with PF on the right side (all dimensions are in mm).

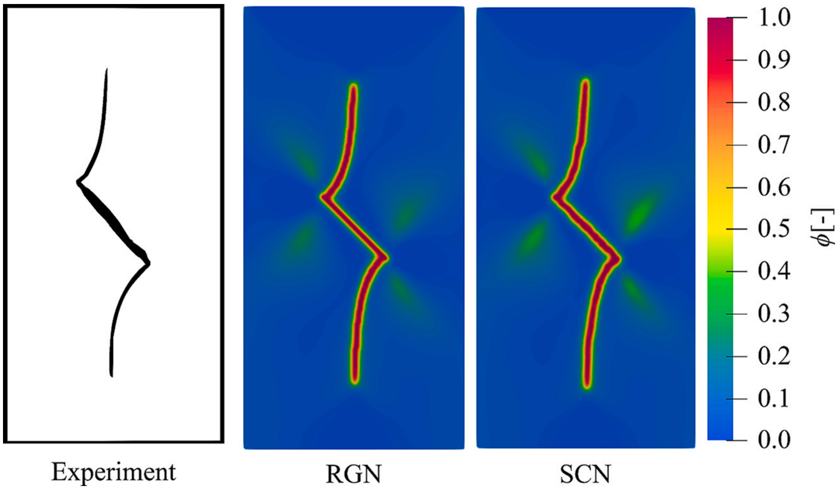

Fig. 27. PF crack propagation under compressive loading obtained with RGN and SCN and its comparison with the reproduced experimental crack path of sample 2 in [71].

In the first test case, a symmetric double-edge cracked plate subjected to tensile loadings is considered. Due to high gradients and the oscillations on the boundaries produced by the traction-free boundary conditions, non-physical crack propagation occurs. Physically correct crack propagation was shown using the boundary stabilization technique proposed in [74]; the results agree well with the reference solution. An essential aspect of splitting the strain energy density is verified. Under the tensile loadings, strain decomposition is unnecessary, as it produces the same results with or without the decomposition of strains. The coalescence phenomenon is shown midway between the cracks if large loading steps are utilized. Otherwise, the coalescence can be seen on one side of the plate if small loading steps are used because of the uneven stress distribution or numerical artefacts. It is also shown that using a smaller loading step does not need any internal iterations because the results with only one iteration are comparable with the iterative process, with less computational cost. The effects of the adaptive loading step size revealed that using the adaptive loading step size requires less computational time than using constant loading steps. At the same time, the numerical accuracy remains the same. The effects of the RGN and SCN are also shown using the adaptive loading step size. The SCN performs well, and the results agree with the RGN. At the end of the first case, an h-convergence study is conducted for RGN and SCN, showing a second-degree convergence. Therefore, the method converges consistent with the second-order augmentation used with the PHSs.

The second case shows the method's performance for a single-edge cracked square plate under shear loadings. Since the PFM is highly sensible to both the mesh size and the numerical method used for the computations, the results of this case were compared with three different solutions obtained with the same material properties. The iterative process results fall between three reference solutions, showing the best agreement with the "Yu et al." [85] reference solutions. Next, the effects of the decomposition of the strain history field are shown. A crack bifurcation can be seen using the strain without splitting it into compressive and tensile parts. It was concluded that a specimen under shear loading produces physically incorrect results if the strain decomposition is not carried out. Therefore, it is mandatory to utilize strain decomposition for any case under shear/mix mode loading conditions. This study uses a spectral split for strains, and the results agree well with the reference solution. The effects of the iterative process show that the iterative process is independent of the loading step size; that is, using a larger loading step (like $\Delta u = 1 \times 10^{-4}$mm) or a smaller loading step (like $\Delta u = 1 \times 10^{-5}$mm) produces the same results, but the iterative process is computationally expensive due to a high number of internal iterations.

In contrast, if a smaller loading step size is used with a non-iterative process, then the results are comparable in accuracy with the iterative process with high computational efficiency compared to the iterative process. Therefore, the non-iterative process was utilized for simulations with a smaller loading step size. To further decrease the computational time, an adaptive loading step size is used, and it is concluded that the adaptive loading step size requires less computational time compared to an iterative process with a constant loading step size. The proposed method performs well when using RGN or SCN. The crack evolution and the corresponding displacement field were also shown. At the end of the second test case, the h-convergence for the displacement field shows a second-degree convergence rate.

The third test case is a rectangular plate with a centrally inclined crack subjected to compressive loads. This test case shows the LRBFCM's ability to handle mixed-mode crack propagation. The results were compared with the experimental crack path, and a good agreement was reached. The above test cases and h-convergence tests show the robustness and accuracy of the proposed strong-form meshless LRBFCM for crack propagation with differently oriented loading and boundary condition types. The limitation of the current work is that it is computationally expensive due to the requirement of very dense nodes. In the future, this computation time can be somewhat reduced while using the variable or adaptive node density near the crack propagation path. One of the possibilities for doing this is the strategy described in [95] for accelerating the LRBFCM in PF simulations. This study will be extended to crack propagation under complex loading conditions like thermo-mechanical crack propagation and different material models.

CRediT authorship contribution statement

Izaz Ali: Writing – original draft, Visualization, Validation, Software, Resources, Methodology, Investigation, Formal analysis, Data curation, Conceptualization. **Gašper Vuga:** Writing – review & editing, Methodology, Conceptualization. **Boštjan Mavrič:** Writing – review & editing, Supervision, Software, Methodology, Conceptualization. **Božidar Šarler:** Writing – review & editing, Supervision, Resources, Project administration, Methodology, Conceptualization.

Declaration of competing interest

The authors declare that they have no known competing financial interests or personal relationships that could have appeared to influence the work reported in this paper.

Acknowledgements

The Slovenian Research and Innovation Agency (ARIS) has supported this work in the framework of the Young Researcher Program, program group P2-0162, projects J2-4477, and L2-3173 cofinanced by Štore-Steel Company (www.store-steel.si).

Data availability

The data will be available upon request.

References

[1] Ali I, Vuga G, Mavrič B, Hanoglu U, Šarler B. Fourth-order phase field modelling of brittle fracture with strong form meshless method. Eng Anal Bound Elem 2024;169:106025. https://doi.org/10.1016/j.enganabound.2024.106025.

[2] Griffith AA. The phenomena of rupture and flow in solids. Philos Trans R Soc Lond Ser Contain Pap Math Phys Character 1921;221:163–98. https://doi.org/10.1098/rsta.1921.0006.

[3] Egger A, Pillai U, Agathos K, Kakouris E, Chatzi E, Aschroft IA, et al. Discrete and phase field methods for linear elastic fracture mechanics: a comparative study and state-of-the-art review. Appl Sci 2019;9:2436. https://doi.org/10.3390/app9122436.

[4] Francfort GA, Marigo J-J. Revisiting brittle fracture as an energy minimization problem. J Mech Phys Solids 1998;46:1319–42. https://doi.org/10.1016/S0022-5096(98)00034-9.

[5] Miehe C, Welschinger F, Hofacker M. Thermodynamically consistent phase-field models of fracture: variational principles and multi-field FE implementations. Int J Numer Methods Eng 2010;83:1273–311. https://doi.org/10.1002/nme.2861.

[6] Ye J-Y, Ballarini R, Zhang L-W. A nonlinear and rate-dependent fracture phase field framework for multiple cracking of polymer. Comput Methods Appl Mech Eng 2023;410:116017. https://doi.org/10.1016/j.cma.2023.116017.

[7] Xu B, Xu T, Heap MJ, Kushnir ARL, Su B, Lan X. An adaptive phase field approach to 3D internal crack growth in rocks. Comput Geotech 2024;173:106551. https://doi.org/10.1016/j.compgeo.2024.106551.

[8] Li Y, Yu T, Xing C, Natarajan S. Crack growth in homogeneous media using an adaptive isogeometric fourth-order phase-field model. Comput Methods Appl Mech Eng 2023;413:116122. https://doi.org/10.1016/j.cma.2023.116122.

[9] Goswami S, Anitescu C, Rabczuk T. Adaptive fourth-order phase field analysis for brittle fracture. Comput Methods Appl Mech Eng 2020;361:112808. https://doi.org/10.1016/j.cma.2019.112808.

[10] Borden MJ, Hughes TJR, Landis CM, Verhoosel CV. A higher-order phase-field model for brittle fracture: formulation and analysis within the isogeometric analysis framework. Comput Methods Appl Mech Eng 2014;273:100–18. https://doi.org/10.1016/j.cma.2014.01.016.

[11] Mandal TK, Nguyen VP, Wu J-Y. On a new high order phase field model for brittle and cohesive fracture: numerical efficiency, length scale convergence and crack kinking. Comput Mater Sci 2022;203:111079. https://doi.org/10.1016/j.commatsci.2021.111079.

[12] Aurojyoti P, Rajagopal A. Fourth order phase field modeling of brittle fracture by Natural element method. Int J Fract 2024. https://doi.org/10.1007/s10704-024-00773-8.

[13] Prusty A, Rajagopal A. Modeling fracture in brittle materials by higher-order phase field method using C^1 non-Sibsonian interpolants. Eng Comput 2023;40:1508–41. https://doi.org/10.1108/EC-12-2022-0735.

[14] Nguyen KD, Thanh C-L, Vogel F, Nguyen-Xuan H, Abdel-Wahab M. Crack propagation in quasi-brittle materials by fourth-order phase-field cohesive zone model. Theor Appl Fract Mech 2022;118:103236. https://doi.org/10.1016/j.tafmec.2021.103236.

[15] Svolos L, Mourad HM, Manzini G, Garikipati K. A fourth-order phase-field fracture model: formulation and numerical solution using a continuous/discontinuous Galerkin method. J Mech Phys Solids 2022;165:104910. https://doi.org/10.1016/j.jmps.2022.104910.

[16] Li W, Ambati M, Nguyen-Thanh N, Du H, Zhou K. Adaptive fourth-order phase-field modeling of ductile fracture using an isogeometric-meshfree approach. Comput Methods Appl Mech Eng 2023;406:115861. https://doi.org/10.1016/j.cma.2022.115861.

[17] Nguyen-Thanh N, Rabczuk T. Phase-field modeling of anisotropic crack propagation based on higher-order nonlocal operator theory. Int J Solids Struct 2024;289:112632. https://doi.org/10.1016/j.ijsolstr.2023.112632.

[18] Nguyen-Thanh N, Zhang Q, Li W, Wu MS, Li S, Zhou K. Higher-order nonlocal operator theory for phase-field modeling of ductile fracture in elasto-plastic materials. Comput Methods Appl Mech Eng 2023;414:116054. https://doi.org/10.1016/j.cma.2023.116054.

[19] Wang R, Wang G, Yang X, Sun F, Huang J, Liao M, et al. Explicit finite element material point method coupled with phase-field model for solid brittle fracture. Eng Fract Mech 2025;316:110865. https://doi.org/10.1016/j.engfracmech.2025.110865.

[20] Zhang P, Kai M-F, Hu X-F, Dai J-G. A phase field model for mixed-mode cohesive failure through fracture energy dissipation at crack surfaces. Eng Fract Mech 2025;316:110869. https://doi.org/10.1016/j.engfracmech.2025.110869.

[21] Tsakmakis A, Vormwald M. Numerical analysis of a phase field model for ductile fracture phenomena. Eng Fract Mech 2025;316:110859. https://doi.org/10.1016/j.engfracmech.2025.110859.

[22] Zhao D, Li B, Storm J, Kaliske M. A comparative study of the representative crack element method and the Star-convex approach within phase-field fracture modeling. Eng Fract Mech 2025;320:111041. https://doi.org/10.1016/j.engfracmech.2025.111041.

[23] Saberi H, Saberi H, Quoc Bui T, Heider Y, Ngoc Nguyen M. A multi-level adaptive mesh refinement method for phase-field fracture problems. Theor Appl Fract Mech 2023;125:103920. https://doi.org/10.1016/j.tafmec.2023.103920.

[24] Wang F, Shao J, Huang H. A phase-field modeling method for the mixed-mode fracture of brittle materials based on spectral decomposition. Eng Fract Mech 2021;242:107473. https://doi.org/10.1016/j.engfracmech.2020.107473.

[25] Staroselsky A, Acharya R, Cassenti B. Phase field modeling of fracture and crack growth. Eng Fract Mech 2019;205:268–84. https://doi.org/10.1016/j.engfracmech.2018.11.007.

[26] Liu J, Xue Y, Zhang Q, Yao K, Liang X, Wang S. Micro-cracking behavior of shale matrix during thermal recovery: insights from phase-field modeling. Eng Fract Mech 2020;239:107301. https://doi.org/10.1016/j.engfracmech.2020.107301.

[27] Qiu S, Duan Q, Shao Y, Chen S, Yao W. Adaptive finite element method for hybrid phase-field modeling of three-dimensional cracks. Eng Fract Mech 2022;271:108636. https://doi.org/10.1016/j.engfracmech.2022.108636.

[28] Wang T, Han H, Wang Y, Ye X, Huang G, Liu Z, et al. Simulation of crack patterns in quasi-brittle materials under thermal shock using phase field and cohesive zone models. Eng Fract Mech 2022;276:108889. https://doi.org/10.1016/j.engfracmech.2022.108889.

[29] Hao L, Yu H, Zhu S, Shen Z, Shen R, Huang K, et al. A mode-adjustable phase-field model for brittle fracture by regulating distortional crack driving energy. Eng Fract Mech 2022;276:108920. https://doi.org/10.1016/j.engfracmech.2022.108920.

[30] Peng X, Fu Z, Zhang Z, Chen S, Ji E, Zhong Q. Two different phase field models of the explicit material point method for brittle dynamic fracture. Eng Fract Mech 2023;290:109449. https://doi.org/10.1016/j.engfracmech.2023.109449.

[31] Hirshikesh D, Schneider B. Nestler, Realization of adaptive mesh refinement for phase-field model of thermal fracture within the FEniCS framework. Eng Fract Mech 2023;293:109676. https://doi.org/10.1016/j.engfracmech.2023.109676.

[32] Suchan T, Kandekar C, Weber WE, Welker K. Crack propagation in anisotropic brittle materials: from a phase-field model to a shape optimization approach. Eng Fract Mech 2024;303:110065. https://doi.org/10.1016/j.engfracmech.2024.110065.

[33] Unnikrishna Pillai A, Behera AK, Rahaman MM. A phase-field length scale insensitive mode-dependent fracture model for brittle failure. Eng Fract Mech 2024;309:110385. https://doi.org/10.1016/j.engfracmech.2024.110385.

[34] Li P, Qiu W, Wu J, Wu Y, Hu K, Zhao L. Fourth-order phase field modeling of dynamic fracture in porous brittle materials using an adaptive isogeometric analysis. Eng Fract Mech 2025;315:110763. https://doi.org/10.1016/j.engfracmech.2024.110763.

[35] Nguyen KD, Augarde CE, Coombs WM, Nguyen-Xuan H, Abdel-Wahab M. Non-conforming multipatches for NURBS-based finite element analysis of higher-order phase-field models for brittle fracture. Eng Fract Mech 2020;235:107133. https://doi.org/10.1016/j.engfracmech.2020.107133.

[36] Ma R, Sun W. FFT-based solver for higher-order and multi-phase-field fracture models applied to strongly anisotropic brittle materials. Comput Methods Appl Mech Eng 2020;362:112781. https://doi.org/10.1016/j.cma.2019.112781.

[37] Wu J, Wang D, Lin Z, Qi D. An efficient gradient smoothing meshfree formulation for the fourth-order phase field modeling of brittle fracture. Comput Part Mech 2020;7:193–207. https://doi.org/10.1007/s40571-019-00240-5.

[38] Amiri F, Millán D, Arroyo M, Silani M, Rabczuk T. Fourth order phase-field model for local max-ent approximants applied to crack propagation. Comput Methods Appl Mech Eng 2016;312:254–75. https://doi.org/10.1016/j.cma.2016.02.011.

[39] Zhang W, Shen Z, Ren J, Gan L, Xu L, Sun Y. Phase-field simulation of crack propagation in quasi-brittle materials: COMSOL implementation and parameter sensitivity analysis. Model Simul Mater Sci Eng 2021;29:055020. https://doi.org/10.1088/1361-651X/ac03a4.

[40] Dong X, Hirshikesh T, Yu Q, Zhang SN. A framework to model freeze/thaw-induced crack propagation in concrete based on a fatigue phase-field method. Eng Fract Mech 2024;306:110260. https://doi.org/10.1016/j.engfracmech.2024.110260.

[41] Navidtehrani Y, Betegón C, Martínez-Pañeda E. A unified abaqus implementation of the phase field fracture method using only a user material subroutine. Materials 2021;14:1913. https://doi.org/10.3390/ma14081913.

[42] Msekh MA, Sargado JM, Jamshidian M, Areias PM, Rabczuk T. Abaqus implementation of phase-field model for brittle fracture. Comput Mater Sci 2015;96:472–84. https://doi.org/10.1016/j.commatsci.2014.05.071.

[43] Molnár G, Gravouil A. 2D and 3D Abaqus implementation of a robust staggered phase-field solution for modeling brittle fracture. Finite Elem Anal Des 2017;130:27–38. https://doi.org/10.1016/j.finel.2017.03.002.

[44] Yu X, Wang R, Dong C, Ji J, Zhen X. 3D implementation of push-out test in ABAQUS using the phase-field method. J Mech Sci Technol 2023;37:1731–45. https://doi.org/10.1007/s12206-023-0314-z.

[45] Behera AK, Unnikrishna Pillai A, Rahaman MM. A phase-field model for electro-mechanical fracture with an open-source implementation of it using Gridap in Julia. Math Mech Solids 2023;28:1877–908. https://doi.org/10.1177/10812865221133860.

[46] Prakash V, Behera AK, Rahaman MM. A phase-field model for thermo-mechanical fracture. Math Mech Solids 2023;28:533–61. https://doi.org/10.1177/10812865221085198.

[47] Unnikrishna Pillai A, Behera AK, Rahaman MM. Combined diffused material interface and hybrid phase-field model for brittle fracture in heterogeneous composites. Eng Fract Mech 2023;277:108957. https://doi.org/10.1016/j.engfracmech.2022.108957.

[48] Hirshikesh, Pramod ALN, Annabattula RK, Ooi ET, Song C, Natarajan S. Adaptive phase-field modeling of brittle fracture using the scaled boundary finite element method. Comput Methods Appl Mech Eng 2019;355:284–307. https://doi.org/10.1016/j.cma.2019.06.002.

[49] Hirshikesh, Natarajan S, Annabattula RK. A FEniCS implementation of the phase field method for quasi-static brittle fracture. Front Struct Civ Eng 2019;13:380–96. https://doi.org/10.1007/s11709-018-0471-9.

[50] Dsouza SM, Hirshikesh TV, Mathew IV, Singh SN. A non-intrusive stochastic phase field method for crack propagation in functionally graded materials. Acta Mechanica 2021;232:2555–74. https://doi.org/10.1007/s00707-021-02956-z.

[51] Borden MJ, Verhoosel CV, Scott MA, Hughes TJR, Landis CM. A phase-field description of dynamic brittle fracture. Comput Methods Appl Mech Eng 2012;217–220:77–95. https://doi.org/10.1016/j.cma.2012.01.008.

[52] Ambati M, Gerasimov T, De Lorenzis L. A review on phase-field models of brittle fracture and a new fast hybrid formulation. Comput Mech 2015;55:383–405. https://doi.org/10.1007/s00466-014-1109-y.

[53] Zhou JX, Li ME. Solving phase field equations using a meshless method. Commun Numer Methods Eng 2006;22:1109–15. https://doi.org/10.1002/cnm.873.

[54] Gomez H, Reali A, Sangalli G. Accurate, efficient, and (iso)geometrically flexible collocation methods for phase-field models. J Comput Phys 2014;262:153–71. https://doi.org/10.1016/j.jcp.2013.12.044.

[55] Dobravec T, Mavrič B, Zahoor R, Šarler B. A coupled domain–boundary type meshless method for phase-field modelling of dendritic solidification with the fluid flow. Int J Numer Methods Heat Fluid Flow 2023;33:2963–81. https://doi.org/10.1108/HFF-03-2023-0131.

[56] Dobravec T, Mavrič B, Šarler B. Reduction of discretisation-induced anisotropy in the phase-field modelling of dendritic growth by meshless approach. Comput Mater Sci 2020;172:109166. https://doi.org/10.1016/j.commatsci.2019.109166.

[57] Talat N, Mavrič B, Belšak G, Hatić V, Bajt S, Šarler B. Development of meshless phase field method for two-phase flow. Int J Multiph Flow 2018;108:169–80. https://doi.org/10.1016/j.ijmultiphaseflow.2018.06.003.

[58] Rana KB, Mavrič B, Zahoor R, Šarler B. Phase-field formulated meshless simulation of axisymmetric Rayleigh-Taylor instability problem. Eng Anal Bound Elem 2024;169:105953. https://doi.org/10.1016/j.enganabound.2024.105953.

[59] Shao Y, Duan Q, Qiu S. Consistent element-free Galerkin method for three-dimensional crack propagation based on a phase-field model. Comput Mater Sci 2020;179:109694. https://doi.org/10.1016/j.commatsci.2020.109694.

[60] Šarler B, Vertnik R. Meshfree explicit local radial basis function collocation method for diffusion problems. Comput Math Appl 2006;51:1269–82. https://doi.org/10.1016/j.camwa.2006.04.013.

[61] Ali I, Hanoglu U, Vertnik R, Šarler B. Assessment of local radial basis function collocation method for diffusion problems structured with multiquadrics and polyharmonic splines. Math Comput Appl 2024;29:23. https://doi.org/10.3390/mca29020023.

[62] G. Vuga, B. Mavrič, B. Šarler, An improved local radial basis function method for solving small-strain elasto-plasticity, (2023). https://doi.org/10.48550/ARXIV.2308.03817.

[63] Mavrič B, Šarler B. Local radial basis function collocation method for linear thermoelasticity in two dimensions. Int J Numer Methods Heat Fluid Flow 2015;25:1488–510. https://doi.org/10.1108/HFF-11-2014-0359.

[64] Hanoglu U, Šarler B. Multi-pass hot-rolling simulation using a meshless method. Comput Struct 2018;194:1–14. https://doi.org/10.1016/j.compstruc.2017.08.012.

[65] Vuga G, Mavrič B, Šarler B. Strong-form meshless numerical modelling of visco-plastic material. Eng Anal Bound Elem 2024;167:105868. https://doi.org/10.1016/j.enganabound.2024.105868.

[66] Rana KB, Mavrič B, Zahoor R, Sarler B. A meshless solution of the compressible viscous flow in axisymmetric tubes with varying cross-sections. Eng Anal Bound Elem 2022;143:340–52. https://doi.org/10.1016/j.enganabound.2022.06.029.

[67] Vuga G, Mavrič B, Šarler B. A hybrid radial basis function-finite difference method for modelling two-dimensional thermo-elasto-plasticity, part 1: method formulation and testing. Eng Anal Bound Elem 2024;159:58–67. https://doi.org/10.1016/j.enganabound.2023.11.014.

[68] Vuga G, Mavrič B, Hanoglu U, Šarler B. A hybrid radial basis function-finite difference method for modelling two-dimensional thermo-elasto-plasticity, Part 2: application to cooling of hot-rolled steel bars on a cooling bed. Eng Anal Bound Elem 2024;159:331–41. https://doi.org/10.1016/j.enganabound.2023.12.001.

[69] Miehe C, Hofacker M, Welschinger F. A phase field model for rate-independent crack propagation: robust algorithmic implementation based on operator splits. Comput Methods Appl Mech Eng 2010;199:2765–78. https://doi.org/10.1016/j.cma.2010.04.011.

[70] Bourdin B, Francfort GA, Marigo J-J. Numerical experiments in revisited brittle fracture. J Mech Phys Solids 2000;48:797–826. https://doi.org/10.1016/S0022-5096(99)00028-9.

[71] Hesammokri P, Isaksson P. Numerical analyses of brittle crack growth experiments in compression using a modified phase-field theory. Int J Solids Struct 2024;296:112815. https://doi.org/10.1016/j.ijsolstr.2024.112815.

[72] Flyer N, Fornberg B, Bayona V, Barnett GA. On the role of polynomials in RBF-FD approximations: I. Interpolation and accuracy. J Comput Phys 2016;321:21–38. https://doi.org/10.1016/j.jcp.2016.05.026.

[73] Bayona V, Flyer N, Fornberg B. On the role of polynomials in RBF-FD approximations: III. Behavior near domain boundaries. J Comput Phys 2019;380:378–99. https://doi.org/10.1016/j.jcp.2018.12.013.

[74] Vuga G, Mavrič B, Šarler B. An improved local radial basis function method for solving small-strain elasto-plasticity. Comput Methods Appl Mech Eng 2024;418:116501. https://doi.org/10.1016/j.cma.2023.116501.

[75] Bayona V, Flyer N, Fornberg B, Barnett GA. On the role of polynomials in RBF-FD approximations: II. Numerical solution of elliptic PDEs. J Comput Phys 2017;332:257–73. https://doi.org/10.1016/j.jcp.2016.12.008.

[76] Shu C, Ding H, Yeo KS. Local radial basis function-based differential quadrature method and its application to solve two-dimensional incompressible Navier–Stokes equations. Comput Methods Appl Mech Eng 2003;192:941–54. https://doi.org/10.1016/S0045-7825(02)00618-7.

[77] Zheng H, Yang Z, Zhang Ch, Tyrer M. A local radial basis function collocation method for band structure computation of phononic crystals with scatterers of arbitrary geometry. Appl Math Model 2018;60:447–59. https://doi.org/10.1016/j.apm.2018.03.023.

[78] Liu X, Liu GR, Tai K, Lam KY. Radial point interpolation collocation method (RPICM) for partial differential equations. Comput Math Appl 2005;50:1425–42. https://doi.org/10.1016/j.camwa.2005.02.019.

[79] Zheng H, Zhang C, Wang Y, Sladek J, Sladek V. A meshfree local RBF collocation method for anti-plane transverse elastic wave propagation analysis in 2D phononic crystals. J Comput Phys 2016;305:997–1014. https://doi.org/10.1016/j.jcp.2015.10.020.

[80] Martin B, Fornberg B, St-Cyr A. Seismic modeling with radial-basis-function-generated finite differences. Geophysics 2015;80:T137–46. https://doi.org/10.1190/geo2014-0492.1.

[81] Gerace S, Erhart K, Kassab A, Divo E. A model-integrated localized collocation meshless method for large scale three-dimensional heat transfer problems. Eng Anal Bound Elem 2014;45:2–19. https://doi.org/10.1016/j.enganabound.2014.01.014.

[82] Dobravec T, Mavrič B, Šarler B, A study on different implementations of Neumann boundary conditions in the meshless RBF-FD method for the phase-field modelling of dendrite growth, Eng. Anal. Bound. Elem. (n.d.). https://doi.org/10.1016/j.enganabound.2025.106154.

[83] Yu Y, Hou C, Zheng X, Rabczuk T, Zhao M. An efficient and robust staggered scheme based on adaptive time field for phase field fracture model. Eng Fract Mech 2024;301:110025. https://doi.org/10.1016/j.engfracmech.2024.110025.

[84] Wu J-Y, Nguyen VP, Nguyen CT, Sutula D, Sinaie S, Bordas SPA. Phase-field modeling of fracture, in: Adv. Appl. Mech., Elsevier, 2020: pp. 1–183. https://doi.org/10.1016/bs.aams.2019.08.001.

[85] Yu Y, Hou C, Zheng X, Rabczuk T, Zhao M. A generally variational phase field model of fracture. Theor Appl Fract Mech 2023;128:104111. https://doi.org/10.1016/j.tafmec.2023.104111.

[86] Weinberg K, Hesch C. A high-order finite deformation phase-field approach to fracture. Contin Mech Thermodyn 2017;29:935–45. https://doi.org/10.1007/s00161-015-0440-7.

[87] Li G, Zhang M, Zhou J. A phase field model with modified volumetric-deviatoric decomposition for the mixed-mode fracture of rock. Comput Geotech 2024;176:106738. https://doi.org/10.1016/j.compgeo.2024.106738.

[88] Hesch C, Weinberg K. Thermodynamically consistent algorithms for a finite-deformation phase-field approach to fracture. Int J Numer Methods Eng 2014;99:906–24. https://doi.org/10.1002/nme.4709.

[89] Fasshauer GE. Meshfree Approximation Methods with Matlab: (With CD-ROM), WORLD SCIENTIFIC, 2007. https://doi.org/10.1142/6437.

[90] Wendland H. Scattered Data Approximation, 1st ed., Cambridge University Press, 2004. https://doi.org/10.1017/CBO9780511617539.

[91] Dyskin AV, Sahouryeh E, Jewell RJ, Joer H, Ustinov KB. Influence of shape and locations of initial 3-D cracks on their growth in uniaxial compression. Eng Fract Mech 2003;70:2115–36. https://doi.org/10.1016/S0013-7944(02)00240-0.

[92] Yang S-Q, Jing H-W. Strength failure and crack coalescence behavior of brittle sandstone samples containing a single fissure under uniaxial compression. Int J Fract 2011;168:227–50. https://doi.org/10.1007/s10704-010-9576-4.

[93] Si Z, Hirshikesh T, Yu W, Fang SN. Mixed-mode thermo-mechanical fracture: an adaptive multi-patch isogeometric phase-field cohesive zone model. Comput Methods Appl Mech Eng 2024;431:117330. https://doi.org/10.1016/j.cma.2024.117330.

[94] Zhou S, Zhuang X, Zhu H, Rabczuk T. Phase field modelling of crack propagation, branching and coalescence in rocks. Theor Appl Fract Mech 2018;96:174–92. https://doi.org/10.1016/j.tafmec.2018.04.011.

[95] Dobravec T, Mavrič B, Šarler B. Acceleration of RBF-FD meshless phase-field modelling of dendritic solidification by space-time adaptive approach. Comput Math Appl 2022;126:77–99. https://doi.org/10.1016/j.camwa.2022.09.008.